

# Structure of quantum vortex tangle in $^4\text{He}$ counterflow turbulence

Luiza Kondaurova<sup>1</sup>, Victor L'vov<sup>2</sup>, Anna Pomyalov<sup>2</sup> and Itamar Procaccia<sup>2</sup>

<sup>1</sup>*Institute of Thermophysics, Novosibirsk, Russia*

<sup>2</sup>*Department of Chemical Physics, The Weizmann Institute of Science, Rehovot 76100, Israel*

The main goal of this paper is to present a comprehensive characterization of well developed vortex tangles in a turbulent counterflow in quantum fluids (with a laminar normal fluid component). We analyze extensive numerical simulations using the vortex filament method, solving the full Biot-Savart equations for the vortex dynamics in a wide range of temperatures and counter-flow velocities. In addition to a detailed analysis of traditional characteristics such as vortex line density, anisotropic and curvature parameters of the vortex tangle, we stress other dynamical and statistical characteristics which are either much less studied or even unstudied. The latter include reconnection rates, mean mutual friction forces, drift velocities and the probability distribution functions of various tangle parameters: the loop length, the line curvature, the mean curvature of loops with a given length, etc. During these studies we compare the three main reconnection procedures which are widely used in the literature, and identify which properties are strongly affected by the choice of the reconnection criteria and which of them are practically insensitive to the reconnection procedure. The conclusion is that the vortex filament method in the framework of the Biot-Savart equation sufficiently robust and well suited for the description of the steady state vortex tangle in a quantum counterflow. The Local-Induction Approximation to this equation may be successfully used to analytically establish relationships between mean characteristics of the stochastic vortex tangle.

## Contents

<b>Introduction</b>	2	A. Evolution of the tangle toward steady state	9
<b>I. Statistical description of the vortex tangle</b>	4	B. Tangle visualization and intervortex distance	11
A. Abbreviations and main notations	4	C. Reconnection dynamics	11
B. Statistical characteristics of the vortex tangle	5	<b>IV. Mean characteristics of the tangle</b>	12
1. The vortex line density $\mathcal{L}$ and the parameter $\gamma$	5	A. Vortex line density $\mathcal{L}$	12
2. Reconnection dynamics and parameter $c_r$	5	1. Numerical results for $\mathcal{L}$ vs. counterflow velocity	12
3. Anisotropy of the vortex tangle and the indices $I_{  }, I_{\perp}, I_{\ell}, I_{\ell\perp}$	5	2. Comparison of numerical and experimental results	12
4. Mean, RMS curvatures $\overline{\mathcal{S}}, \tilde{\mathcal{S}}$ and parameters $c_1, c_2$	5	3. Dependence of numerical results for vortex line density on reconnection criteria	13
5. Drift velocity of the vortex tangle $V_{vt}$ and parameter $C_{vt}$	6	4. Phenomenological analysis of $\gamma(T)$	14
6. Friction force density and the Gorter-Mellink constant	6	5. Intercept velocity	15
7. Autocorrelation of the vortex orientations	6	B. Mean tangle anisotropy	15
<b>II. Vortex Filament Method</b>	6	C. Mean and RMS vortex-line curvature	16
A. Basic Equations and their implementation	6	D. Drift velocity of the vortex tangle $V_{vt}$	16
1. Equations of motion of the vortex line	6	E. Mutual friction force $F_{ns}$	17
2. Local Induction Approximation	7	F. Mean and most probable loop lengths	18
3. Implementation of the full Biot Savart velocity	7	<b>V. Detailed statistics of the vortex tangle</b>	18
B. Criteria of vortex reconnection	8	A. Probability density function (PDF) of vortex-loop lengths	18
1. Schwartz's geometrical criterion in LIA	8	B. PDF of the line-curvature	18
2. Other geometric criteria for full Biot-Savart equations	8	C. Correlation between loop length $l_j$ and RMS of the loop curvature $\tilde{s}_j''$	19
3. Dynamical criterion	8	D. PDFs of the mean and RMS loop curvature	20
C. Implementation Details	9	E. Autocorrelation of the vortex orientation	22
<b>III. Dynamics of the vortex tangle</b>	9	<b>VI. On the physics of <math>^4\text{He}</math> counterflow turbulence</b>	23
		A. Idealizations and relevant parameters	23
		1. Spatial homogeneity	23
		2. No isotropy, just axial symmetry	23

3. The physical parameters of the problem	24
B. $V_{\text{ns}}$ -dependence of the vortex-tangle characteristics	24
C. Schwartz's bridge relations	24
D. Probability distribution and correlation functions in the vortex tangle	25
E. Dynamical and statistical characteristics vs. reconnection criteria	25
<b>Acknowledgments</b>	26
<b>References</b>	26

## Introduction

The term “quantum turbulence” or “superfluid turbulence” refers to a tangle of interacting quantized vortex lines, which are formed, for example, in superfluid  $^4\text{He}$ ,  $^3\text{He}$  or in Bose-Einstein condensates of ultra-cold atoms. The vorticity in superfluids is restricted to a set of vortex lines around which the circulation is quantized to multiples of the circulation quantum  $\kappa = h/m$ . Here  $h$  is Planck’s constant and  $m$  is mass of either atoms with integer spin, like  $^4\text{He}$  or Cooper pairs of  $^3\text{He}$  atoms. The creation of sustained quantum turbulence can be achieved by either mechanical excitations [1–8], or by heat currents (so-called counterflow turbulence). Experimental studies of thermal counterflow, initiated almost sixty years ago by Vinen [9, 10], became the most extensively studied forms of quantum turbulence [11–16].

In the context of the popular two-fluid model of superfluids the phenomenon of thermal counterflow may be considered as consisting of two interpenetrating fluid flows - a normal viscous component flowing in the direction of the temperature gradient and carrying the heat flux, and an inviscid superfluid component flowing in the opposite direction to keep a zero total mass transfer. These two components may have different velocity and density fields. More sophisticated arrangements [17] allow one to realize (mechanically driven) pure superflows in a relatively wide (7-10 mm) channel, with the normal fluid component practically at rest. In both arrangements, a dense vortex tangle is excited under the influence of the velocity difference between the two components quantum turbulence.

Some statistical properties of quantum vortex tangles in counter- and super-flows were studied experimentally and numerically [9–24]. Among seminal contributions to these studies we should mention again a pioneering work by Vinen [9, 10], in which he also suggested a phenomenological description of counterflow turbulence, Eq. (17) and by Schwarz [19], who established some important bridge-relationships between mean characteristics of the vortex tangle and pioneered numerical simulations of the counterflow turbulence mainly in the Local Induction Approximation (see Sec. IIA2). Later Adachi, Fujiyama, and Tsubota [22] demonstrated that for an adequate nu-

merical study of the counterflow turbulence one has to relax this approximation and to use the Biot-Savart equation (10a), according to which each point of the vortex line is swept by the velocity field produced by the entire tangle. The development of the field was recently reviewed in [25–27].

The intensity of quantum turbulence is usually characterized by the vortex line density per unit volume, sometime referred as VLD and denoted by  $\mathcal{L}$ . Another related characteristic is the intervortex distance  $\ell \equiv 1/\sqrt{\mathcal{L}}$ . Other properties of the tangle, such as the mean curvature, scale with  $\ell$  [19].

During temporal evolution vortex lines can collide and reconnect changing the tangle’s topology. Thus vortex loops can merge or break up into smaller loops. These reconnections occur on scales comparable with the vortex core radius and were studied in the approximation of the Gross-Pitaevskii equation [28–33]. This approximation is adequate when the vortex core radius exceeds significantly the interatomic distance, like in  $^3\text{He}$ , but not in the  $^4\text{He}$ . Recently the reconnection events were visualized experimentally [34]. Reconnections play a crucial role in the vortex dynamics. In particular they directly affect the steady state value of  $\ell$ . In typical experimental conditions the vortex tangle is dense in the sense that the intervortex distance  $\ell$  is much smaller than the characteristic size of the experimental cell  $H$ , which is about 1 cm. At the same time the tangle is sparse enough such that  $\ell$  is much larger than the vortex core radius  $a_0$ , which is of the order of  $10^{-8}$  cm in  $^4\text{He}$ . To follow the evolution of the vortex tangle at the intermediate scales  $a_0 \ll \ell \ll H$ , Schwarz [18, 19] proposed to use a vortex filament method (sometime referred to as VFM) in which minor core variations of the quantized vortices are ignored and the vortices are approximated as directional lines with a predefined core structure. If so, the time evolution of these vortex lines is governed by the Biot-Savart equation (10a). Numerically vortex lines may be approximated as a set of small straight vortex filaments described by a directional set of connected points placed at distances much smaller than  $\ell$ .

The Biot-Savart equation for quantized vortices does not describe the vortex reconnections. They are included in vortex filament methods as an additional artificial procedure that changes the connectivity of pairs of points according to some reconnection criterion. Reconnection criteria are based on a physical intuition and the results of numerical simulations. Since the method introduction by Schwarz [18, 19], a number of different criteria [20, 22, 28, 35–38] were introduced and modified over time. Currently, three criteria are frequently used to trigger the reconnections during the evolution of the vortex tangle. These are based either on geometrical proximity [22, 28, 37] or on the dynamics of vortex filaments [38–40], leading to a different number of reconnections and various changes in the vortex tangle topology.

The presence of variety of artificial reconnection procedures in vortex filament methods and the spread in values

of basic characteristics of the tangle, such as the vortex reconnection rates and steady-state vortex line density  $\mathcal{L}$ , resulted in the superfluid community sharing an opinion that was made explicit recently by Skrbek and Sreenivassan [25]: “While it is clear that the full Biot-Savart approach is certainly better [than the Local-Induction Approximation (LIA), see below], there are still other aspects such as approach to vortex reconnections and influence of possible normal fluid turbulence that make the predictive power of these simulations limited at the best.”

In this paper we consider this strong statement as a research challenge, turning it to our main question: “To what extent can one state that the statistical properties of the developed vortex tangles obtained by vortex filament methods (in a wide range of parameters) are robust under changes of the reconnection procedures and other implementation details?”. To answer this question we report in this paper the results of comprehensive numerical simulations of counterflow turbulence for a wide range of parameters: at low, medium and high temperatures  $T$  (1.3, 1.6 and 1.9 K) and the counterflow velocities  $V_{\text{ns}}$  ranging from 0.3 to 1.2 cm/s. For all combinations of temperatures and velocities we compared results of vortex filament method with three different reconnection criteria [22, 31, 40]. We found which properties are strongly affected by the choice of the reconnection criteria (e.g. the reconnection rate differs more than in order of magnitude for different criteria), which properties only relatively weakly depend on this choice (such as mean properties of the tangle) and which are insensitive to it (such as probability distribution functions of local properties). Our results partially agree with preliminary observations by Baggaley [41] who recently compared the values of the vortex line density calculated with a number of reconnection criteria for  $T = 1.6\text{K}$  and  $0.35 < V_{\text{ns}} < 0.65$  cm/s and concluded that the values of  $\mathcal{L}$  are insensitive to the choice of the criterion for these parameters.

The paper is organized as follows: in Section I we describe mean and local statistical characteristics of vortex tangle beginning with a summary of the main notations and abbreviations used in the paper.

Section II is devoted to a brief overview of the vortex filament method. In particular, in Subsec. IIA we present the basic equation of the vortex line motion. In Subsec. IIB we discuss the reconnection criteria and clarify in Subsec. IIC the implementation details.

Our results are presented and discussed in Secs. III, IV and V. In Sec. III we consider the dynamics of the vortex tangle, including its evolution toward steady state and reconnection dynamics with different reconnection criteria. Here we also show the typical tangle configurations for different reconnection criteria.

In Sec. IV we describe the mean characteristics of vortex tangle, starting in Subsec. IB1 with a detailed discussion of the vortex line density and its dependence on the temperature and counterflow velocity in comparison with results of other simulations and laboratory experiments. We also discuss the mean tangle anisotropy, the

mean and RMS vortex line curvatures, the mean friction force between normal and superfluid components, the drift velocity of the vortex tangle and the mean and most probable loop lengths. In some sense this level of description is similar to the thermodynamical approach to gases and fluids that deals with the mean characteristics such as temperature, pressure, density, etc., averaged over finite (physical) volume.

A more advanced description of continuous media was reached in statistical physics and kinetics in the framework of probability distribution functions, PDFs, (e.g. Maxwell-Boltzmann PDF of atomic velocities) and correlation functions (e.g. of atomic positions). Similarly, the measurable mean characteristics of the vortex tangle provide important but very limited information on the tangle properties.

Clearly, PDFs and correlation functions are much more informative and the theoretical description of quantum turbulence definitely calls for such a knowledge, see, e.g. review by Nemirovski [27]. Unfortunately there is not much chance that these details can be subject to experimental study. Therefore numerical characterization of detailed local vortex tangle statistics addressed in Sec. V is important and timing. In particular we show that the core of the PDF of vortex loop length, Eq. (22), and PDF of line curvature, Eq. (23), have exponential form with linear prefactor [ $\propto x \exp(-x)$ ], while PDF of the mean-loop curvature has a Gaussian form Eq. (25) [ $\propto \exp(-x^2)$ ].

We discuss also the correlation between loop length and their mean curvature. Finally we find the autocorrelation of the vortex-line orientation.

The concluding Sec. VI summarizes our view and results on the physical picture of  $^4\text{He}$  counterflow turbulence. It begins in Sec. VIA with a short discussion of standard idealizations and their realizability that determine the set of relevant physical parameters of the problem. In Sec. VIB, employing dimensional reasoning and (where required) some simple physical arguments, we use the latter to describe the dependence of the basic physical characteristics of the problem on the counterflow velocity. Next we present a detailed summary of our numerical results and list the actual numerical values of the corresponding dimensionless parameters which, according to naïve dimensional reasoning are expected to be of the order of unity.

In the short Sec. VIC we recall relations that stem from the local induction approximation [19] that bridge the vortex line density, the mutual friction force and the tangle drift velocity with the anisotropy and curvature parameters of the tangle. We summarize our results on realizability of these relations in numerical simulation with the full Biot-Savart equations.

In the next Sec. VID we summarize our results on various PDFs that characterize different aspects of the tangle statistics. The last Sec. VIE deals with the dependence of our numerical results on the reconnection criteria and culminates with the optimistic statement:

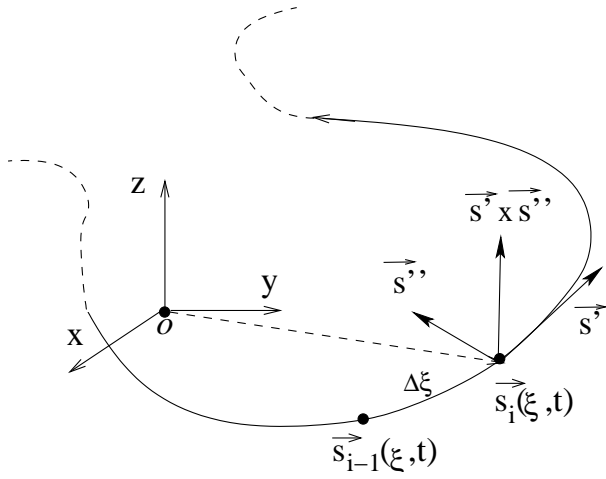


FIG. 1: The coordinate system. The origin of the Cartesian system is placed at the center of the computational box. Each vortex line point  $\mathbf{s}_i$  is defined by Cartesian coordinates  $x_i, y_i, z_i$  and a label  $\xi$  along the line. Vectors  $\mathbf{s}'$ ,  $\mathbf{s}''$  and  $\mathbf{s}' \times \mathbf{s}''$  are the tangential, the local curvature vector and the direction of the local induced velocity, associated with the point  $\mathbf{s}(\xi)$  of the vortex filament, respectively. Primes denote differentiation with respect to the instantaneous arclength  $\xi$ .

At the current level of understanding of the vortex statistics in counterflow turbulence, the vortex filament numerical method in the framework of full Biot-Savart equation (12) provides adequate qualitative and reasonably accurate quantitative information on the quantum vortex dynamics in superfluid turbulence. This information is required for the further development of an adequate physical model of this intriguing phenomenon.

Although local induction approximation to Eq. (12) fails to reproduce accurately vortex tangle properties in numerical studies [22], we demonstrate that analytical relationships between different mean characteristics of the vortex tangles, found in [19] within the LIA framework, are well obeyed in our Biot-Savart simulations. Therefore we think that the Local Induction Approximation may be effectively used in analytical theory of counterflow turbulence.

## I. STATISTICAL DESCRIPTION OF THE VORTEX TANGLE

### A. Abbreviations and main notations

LHS & RHS – left- and right-hand side of equation;

BSE – Biot-Savart equation (10a);

VFM – vortex filament method, Sec. II

LIA – local induction approximation, Sec. II A 2, Eqs. (11);

GC – Geometrical reconnection criterion, Sec. II B 2, Eq. (14);

GEC – Geometric-energetic reconnection criterion, Sec. II B 2;

DC – Dynamical reconnection criterion, Sec. II B 3;

$l_j$  – length of particular  $j$ -loop;

$L_{\text{tot}} = \sum_{j=1}^N l_j$  and  $\bar{L} = L_{\text{tot}}/N$  – total and mean length of the vortex tangle, consisting of  $N$  loops;

VLD – vortex line density of the tangle, occupying volume  $\mathcal{V}$ ,  $\mathcal{L} = L_{\text{tot}}/\mathcal{V}$ , Eq. (1);

$\ell \equiv 1/\sqrt{\mathcal{L}}$  – mean intervortex distance, Eq. (1);

$\mathbf{V}_s$ ,  $\mathbf{V}_n$  and  $\mathbf{V}_{ns} = \mathbf{V}_n - \mathbf{V}_s$  – the macroscopic velocities of super-fluid, normal fluid and counterflow, respectively;

$\mathbf{V}_{vt}$  – mean drift velocity of the vortex tangle with respect to the superfluid rest frame;

$\mathbf{s}(\xi)$  – Cartesian coordinate of the vortex line, parameterized with the arc-length  $\xi$ , Fig. 1;

$\mathbf{s}'(\xi) \equiv d\mathbf{s}/d\xi$  – local direction of the vortex line, Fig. 1;

$\mathbf{s}''(\xi) \equiv d^2\mathbf{s}/d\xi^2$  – local curvature vector, Fig. 1;

$\delta(t)$  – smallest distance between two vortex lines, approaching reconnection;

PDF – probability distribution function  $\mathcal{P}(x)$  of some local characteristics  $x$ , normalized such that  $\int \mathcal{P}(x) dx = 1$ ;

$\mathcal{P}(l)$  &  $\mathcal{P}(|s''|)$  – PDFs of the loop length and of the line curvature

$\bar{X} \equiv \langle x \rangle = \int x \mathcal{P}(x) dx$  – Mean value of  $x$ ;

$\tilde{X} \equiv \sqrt{\langle x^2 \rangle}$  – RMS, Root-mean-square value of  $x$ ;

$L_*$  – Most probable value of the loop length,  $d\mathcal{P}(l)/dl|_{l=L_*} = 0$ .

$\bar{S} \equiv \langle |s''| \rangle$ ,  $\tilde{S} \equiv \sqrt{\langle |s''|^2 \rangle}$  – mean and RMS vortex curvature, Eqs. (5);

$R \equiv 1/\tilde{S}$  – characteristic radius of curvature of the vortex tangle;

$a_0 = 1.3 \times 10^{-8}$  cm – effective core radius of  $^4\text{He}$ ;

$\kappa = 9.97 \times 10^{-4}$  cm<sup>2</sup>/s – circulation quantum;

$\Lambda = \ln [cR/a_0]$ ,  $c = O(1)$ ,  $\tilde{\Lambda} = \Lambda/4\pi$ , – defines the stiffness of the vortex line with respect to bending, Eq. (11);

$\beta = \kappa\tilde{\Lambda}$  – quantify the local contribution to the line point velocity, Eq. (11).

## B. Statistical characteristics of the vortex tangle

### 1. The vortex line density $\mathcal{L}$ and the parameter $\gamma$

Denote the total vortex length in the tangle occupying a volume  $\mathcal{V}$  as  $L_{\text{tot}}$ . Then the vortex line density  $\mathcal{L}$  and mean intervortex distance  $\ell$  can be found as:

$$L_{\text{tot}} = \int_{\mathcal{C}} d\xi, \quad \mathcal{L} \equiv L_{\text{tot}}/\mathcal{V}, \quad \ell \equiv 1/\sqrt{\mathcal{L}}. \quad (1)$$

Here the integral is taken over the whole vortex configuration  $\mathcal{C}$ .

Asserting that  $\kappa$  ( $[\kappa] = \text{cm}^2/\text{s}$ ) is the only relevant parameter in the problem and  $[\mathcal{L}] = 1/\text{cm}^{-2}$  one can employ the counterflow velocity  $V_{\text{ns}}$  in a dimensional argument to write  $\sqrt{\mathcal{L}} \sim V_{\text{ns}}/\kappa$  or:

$$\sqrt{\mathcal{L}} = \frac{\Gamma}{\kappa} V_{\text{ns}}, \quad \gamma \equiv \frac{\Gamma}{\kappa}. \quad (2a)$$

Here  $\Gamma$  is a dimensionless parameter which in general is temperature dependent. Naïvely one expects that  $\Gamma$  is of the order of unity. Numerical and experimental studies (see e.g. our Tab. III) give  $\Gamma \sim 0.1$ .

It is customary to use in relation (2a) a dimensional parameter  $\gamma(T)$  instead of  $\Gamma$ . The parameter  $\gamma$  is the subject of intensive experimental, numerical and theoretical studies and will be discussed in details in Sec. IV A.

In practice most experimental and numerical data of the time averaged steady state value of  $\mathcal{L}$  are approximated by a slightly different form of this equation[13]:

$$\mathcal{L} = \gamma^2 (V_{\text{ns}} - v_0)^2, \quad (2b)$$

which includes an additional fitting parameter, the intercept velocity  $v_0$ .

### 2. Reconnection dynamics and parameter $c_r$

The reconnections between vortex lines lead to the development of a steady state vortex tangle. The statistics of the reconnections is therefore important for characterizing the tangle. In a periodic box only two kinds of reconnection are possible: one vortex loop splits into two smaller loops, or two loops merge into one larger loop. The ratio of the number of reconnection of two types (in a unit volume),  $N_1/N_2$  is shown in Fig. 6.

The second important characteristic of the vortex dynamics is the total reconnection rate  $dN_r/dt$  ( $N_r \equiv N_1 + N_2$ ) in a unit volume. In the steady state the relation between mean reconnection rate  $\langle dN_r \rangle/dt$  and  $\mathcal{L}$  can be found by a simple dimensional argument:  $[\langle dN_r \rangle/dt] = \text{cm}^{-3}\text{s}^{-1}$  may be uniquely expressed via  $[\kappa] = \text{cm}^2/\text{s}$  and  $[\mathcal{L}] = \text{cm}^{-2}$ : [37, 42–44] as

$$\frac{dN_r}{dt} = c_r \kappa \mathcal{L}^{5/2}. \quad (3)$$

Here  $c_r$  is a temperature dependent dimensionless coefficient. One sees in Fig. 7 that the relation (3) is perfectly obeyed in our simulations but the numerical values of  $c_r$ , given in Tab. II, crucially depend on the reconnection criteria. The reasons and consequences of this fact for the final steady state tangle are discussed in Sec. III C.

### 3. Anisotropy of the vortex tangle and the indices $I_{\parallel}, I_{\perp}, I_{\ell}, I_{\ell\perp}$

The presence of the counterflow velocity creates a preferred direction and the vortex tangle is anisotropic. To measure the degree of anisotropy of the tangle Schwarz [19] introduced the anisotropy indices:

$$I_{\parallel} = \frac{1}{L_{\text{tot}}} \int_{\mathcal{C}} [1 - (\mathbf{s}' \cdot \hat{\mathbf{r}}_{\parallel})^2] d\xi, \quad (4a)$$

$$I_{\perp} = \frac{1}{L_{\text{tot}}} \int_{\mathcal{C}} [1 - (\mathbf{s}' \cdot \hat{\mathbf{r}}_{\perp})^2] d\xi, \quad (4b)$$

$$I_{\ell} = \frac{\ell}{L_{\text{tot}}} \int_{\mathcal{C}} \hat{\mathbf{r}}_{\parallel} \cdot (\mathbf{s}' \times \mathbf{s}'') d\xi, \quad (4c)$$

where  $\hat{\mathbf{r}}_{\parallel}$  and  $\hat{\mathbf{r}}_{\perp}$  are unit vectors in the direction parallel and perpendicular to  $\mathbf{V}_{\text{ns}}$ , respectively. In the steady state these indices averaged over time obey relation  $I_{\parallel}/2 + I_{\perp} = 1$ . The index  $I_{\ell}$  measures the mean local velocity (in units  $\kappa/\ell$ ) in the direction of the counterflow. In the isotropic case  $I_{\parallel} = I_{\perp} = 2/3, I_{\ell} = 0$ .

To test the isotropy of the velocity in the direction perpendicular of the counterflow, we also measure

$$I_{\ell\perp} = \frac{\ell}{L_{\text{tot}}} \int_{\mathcal{C}} \hat{\mathbf{r}}_{\perp} \cdot (\mathbf{s}' \times \mathbf{s}'') d\xi, \quad (4d)$$

which is expected to vanish if the velocity is isotropic in the plane perpendicular to the counterflow velocity, even if  $I_{\ell}$  is not small. Our results for the dimensionless anisotropy indices are given in Tab. IV and discussed in Sec. IV B.

### 4. Mean, RMS curvatures $\bar{S}, \tilde{S}$ and parameters $c_1, c_2$

Other important global properties of the vortex tangle are the mean and RMS curvatures  $\bar{S}$  and  $\tilde{S}$ , which may be expressed as an integral over the whole vortex configuration  $\mathcal{C}$ , occupying a volume  $\mathcal{V}$ :

$$\bar{S} \equiv \langle |s''| \rangle = \frac{1}{L_{\text{tot}}} \int_{\mathcal{C}} |s''| d\xi, \quad (5a)$$

$$\tilde{S}^2 \equiv \langle |s''|^2 \rangle = \frac{1}{L_{\text{tot}}} \int_{\mathcal{C}} |s''|^2 d\xi. \quad (5b)$$

These objects are expected to scale with the mean density as [19]:

$$\bar{S} = c_1 \sqrt{\mathcal{L}}, \quad \tilde{S} = c_2 \sqrt{\mathcal{L}}, \quad (5c)$$

where  $c_1$  and  $c_2$  are dimensionless constants of the order of unity (see below Tab. IV).

Similarly we can find the mean and RMS curvature  $\overline{s_j''}$  and  $\tilde{s}_j''$  of a particular vortex loop  $\mathcal{C}_j$  of length  $l_j \equiv \int_{\mathcal{C}_j} d\xi$ :

$$\overline{s_j''} \equiv \langle |s''| \rangle_j = \frac{1}{l_j} \int_{\mathcal{C}_j} |s''| d\xi, \quad (6a)$$

$$\tilde{s}_j''^2 \equiv \langle |s''|^2 \rangle_j = \frac{1}{l_j} \int_{\mathcal{C}_j} |s''|^2 d\xi. \quad (6b)$$

The global (over the entire tangle) PDF of  $|s''|$  and the PDFs of the vortex-loop length,  $l_j$ , the mean-loop curvature,  $\overline{s_j''}$  and the correlations between  $l_j$  and  $\tilde{s}_j''$  are presented and discussed in Sec. V.

#### 5. Drift velocity of the vortex tangle $V_{vt}$ and parameter $C_{vt}$

The drift velocity of the vortex tangle with respect to the superfluid rest frame is

$$\mathbf{V}_{vt} = \frac{1}{L_{tot}} \int \frac{d\mathbf{s}(\xi)}{dt} d\xi - \mathbf{V}_s, \quad (7a)$$

where the velocity of the vortex line point  $d\mathbf{s}(\xi)/dt$  is given below by Eq. (10b). It is natural to expect that  $\mathbf{V}_{vt}$  is proportional to the counterflow velocity  $\mathbf{V}_{ns}$  and to introduce a dimensionless parameter  $C_{vt}$  as their ratio:

$$\mathbf{V}_{vt} = C_{vt} \mathbf{V}_{ns}. \quad (7b)$$

The values of  $C_{vt}$  are discussed in Sec. IV D.

#### 6. Friction force density and the Gorter-Mellink constant

In discussions of the mechanical balance in superfluid turbulence an important role is played by the mutual force density exerted by the normal fluid on the superfluid. It may be found from Eq. (10b) (the term proportional to  $\alpha'$  vanishes by symmetry) [19]

$$\mathbf{F}_{ns} = \rho_s \kappa \alpha J, \quad J \equiv -\frac{1}{V} \int \mathbf{s}' \times [\mathbf{s}' \times (\mathbf{V}_{ns} - \mathbf{V}_{si})] d\xi. \quad (8a)$$

The integral  $J$  [with dimensions  $[J] = 1/(\text{s cm})$ ] may be uniquely expressed via  $\kappa$  and  $V_{ns}$  as  $V_{ns}^3/\kappa^2$ . This leads to the dimensional estimate for  $F_{ns}$

$$F_{ns} = \frac{\alpha \rho_s}{\kappa} (C_f V_{ns})^3, \quad (8b)$$

with a dimensionless temperature dependent constant  $C_f$ . This agrees with the Gorter-Mellink [24] result that reads  $F_{ns} \propto V_{ns}^3$ :

$$F_{ns} = A_{GM} \rho_s \rho_n V_{ns}^3. \quad (8c)$$

Comparing equations (8b) and (8c) one finds the relationship between  $C_f$  and the dimensional Gorter-Mellink constant  $A_{GM}$ :

$$A_{GM} = C_f^3 \frac{\tilde{\alpha}}{\kappa \rho}, \quad \tilde{\alpha} \equiv \alpha \rho / \rho_n. \quad (8d)$$

As is known, the density  $\rho$  of  $^4\text{He}$  varies only weakly with the temperature in the relevant temperature range, while  $\alpha$  varies rapidly. It increases 6 times as  $T$  grows from 1.3 to 1.9 K, see Table I. On the other hand, the temperature dependence of the parameter  $\tilde{\alpha}$ , that actually governs the temperature dependence of  $A_{GM}$ , is much weaker than  $\alpha$ . Further discussion of the friction force density is given below in Sec. IV E.

#### 7. Autocorrelation of the vortex orientations

To test the relative polarization of the vortex lines we measure an orientation correlation function

$$K(\mathbf{r}_1 - \mathbf{r}_2) = \left\langle \mathbf{s}'(r_1) \cdot \mathbf{s}'(r_2) \right\rangle_{\mathcal{C}}, \quad (9)$$

where  $\mathbf{r}_1$  and  $\mathbf{r}_2$  are the Cartesian coordinates of the two line points and we average over all pairs of the line points in the tangle.  $K(\mathbf{r}_1 - \mathbf{r}_2)$  measures the average angle between line segments as a function of the distance between them. Averaged over all distances it quantifies the polarization of the tangle  $\overline{K}$ .

## II. VORTEX FILAMENT METHOD

The vortex filament method and the reconnection criteria were presented in details, e.g. in Refs. [18–22, 28, 40, 41, 45]. Nevertheless, to keep the paper self-contained, and to introduce notations and definitions, we review these criteria with the focus on the underlying physical processes. The basic equations are presented in Sec. II A and the criteria of vortex reconnection are discussed in Sec. II B. A short description of the implementation details is given in Sec. II C.

### A. Basic Equations and their implementation

#### 1. Equations of motion of the vortex line

When no external forces act on the vortex core the vortex line moves with the velocity  $\mathbf{V}_{si}(\mathbf{s})$  defined by the

entire vortex tangle according to the Biot-Savart equation:

$$\mathbf{V}_{\text{si}}(\mathbf{s}) = \frac{\kappa}{4\pi} \int_{\mathcal{C}} \frac{(\mathbf{s}_1 - \mathbf{s}) \times d\mathbf{s}_1}{|\mathbf{s}_1 - \mathbf{s}|^3}. \quad (10a)$$

Here the vortex line is presented in a parametric form  $s(\xi, t)$ , where  $\xi$  is an arclength,  $t$  is the time and the integral is taken over the entire vortex tangle configuration.

In addition to the self-induced velocity of the superfluid component, we have to account for the interaction with the normal component via mutual friction, characterized by two dimensionless temperature dependent parameters  $\alpha$  and  $\alpha'$  [18, 19]:

$$\begin{aligned} \frac{d\mathbf{s}}{dt} = & \mathbf{V}_s + \mathbf{V}_{\text{si}} + \alpha \mathbf{s}' \times (\mathbf{V}_{\text{ns}} - \mathbf{V}_{\text{si}}) \\ & - \alpha' \mathbf{s}' \times \left[ \mathbf{s}' \times (\mathbf{V}_{\text{ns}} - \mathbf{V}_{\text{si}}) \right] + \mathbf{v}_{\text{bc}}. \end{aligned} \quad (10b)$$

Here  $\mathbf{V}_s$  is the macroscopic super-fluid velocity, and the counterflow velocity  $\mathbf{V}_{\text{ns}} = \mathbf{V}_n - \mathbf{V}_s$  is the relative velocity of the superfluid component. In the reference frame co-moving with the superfluid component,  $\mathbf{V}_s = 0$  and the relative velocity equals to the velocity of normal fluid  $\mathbf{V}_{\text{ns}} = \mathbf{V}_n$  in this reference frame. In our simulations  $\mathbf{V}_{\text{ns}}$  is oriented towards the positive  $z$ -direction. The prime in  $\mathbf{s}'$  denotes derivative with respect to the instantaneous arc-length  $\xi$ , e.g.  $\mathbf{s}' = d\mathbf{s}/d\xi$ . The mean velocities obey a mass conservation law  $\rho_s \mathbf{V}_s + \rho_n \mathbf{V}_n = 0$ , where  $\rho_n$  and  $\rho_s$  are the densities of normal and superfluid components respectively. The density  $\rho = \rho_n + \rho_s$  refers to the density of  ${}^4\text{He}$ . The term  $\mathbf{v}_{\text{bc}}$  describes the influence of the boundary conditions. For the periodic boundary conditions used in this work, the line points leaving the box from one side were algorithmically brought back to the computational volume by appropriately shifting their coordinates without changing their velocity  $\dot{\mathbf{s}}(z) = \dot{\mathbf{s}}(z + H)$ ,  $\dot{\mathbf{s}}(y) = \dot{\mathbf{s}}(y + H)$ ,  $\dot{\mathbf{s}}(x) = \dot{\mathbf{s}}(x + H)$ , where  $H$  is the size of the computational domain.

## 2. Local Induction Approximation

Eqs (10a) implies that the vortex line is infinitely thin. Attempting to calculate the velocity at a particular point  $\mathbf{s}$  on the vortex line one finds that the integral logarithmically diverges as  $\mathbf{s}_1 \rightarrow \mathbf{s}$ . To resolve this difficulty one has either to cut the integral at  $|\mathbf{s}_1 - \mathbf{s}| = a_0$  or to account for the particular form of the vortex core structure. Physically it means that  $\mathbf{V}_{\text{si}}(\mathbf{s})$  in the integral (10a) is dominated by the local contributions from the vortex line for which  $a_0 \leq |\mathbf{s}_1 - \mathbf{s}| \leq cR$ . The upper limit of integration is about the mean curvature of the tangle  $R$  determined up to a dimensionless constant  $c$  of the order of unity. Neglecting nonlocal contribution one arrives to

the Local Induction Approximation (LIA)[46, 47]:

$$\mathbf{V}_{\text{si}}^{\text{LIA}} = \beta \mathbf{s}' \times \mathbf{s}'', \quad \beta \equiv \kappa \tilde{\Lambda}, \quad \tilde{\Lambda} \equiv \frac{\Lambda}{4\pi}, \quad (11a)$$

$$\Lambda = \ln \left[ \frac{cR}{a_0} \right] \approx \ln \left[ \frac{\ell}{a_0} \right]. \quad (11b)$$

The value of the ratio of mean local to mean nonlocal contributions to the velocity is about  $\Lambda$ . Besides the traditional parameter  $\Lambda$  we introduce also a frequently used combination  $\tilde{\Lambda}$ . The values of  $\tilde{\Lambda}$  found numerically are very close to unity, see Tab. I.

Notice that Eq. (11a) is integrable, having an infinite number of integrals of motion, including the total line length. Therefore numerical simulations with the full BSE (10a) are not a question of accounting for a small (about 10%) nonlocal contributions to the line velocity, but are required by necessity to account for the violation of infinitely many conservation laws.

Nevertheless one can exploit the fact that the local contribution (11a) to the vortex velocity does dominate the non-local one and to use the simple local relation (11a) in analytical studies of the vortex tangle characteristics, for example, in the way developed by Schwarz [19]. He established a set of bridge relations between different mean characteristics of the vortex tangle. In Secs. IV A 4, IV D and IV E we demonstrate that these relations are well obeyed by the mean vortex characteristics found directly from numerical simulations in the framework of the VFM with full Biot-Savart equations.

## 3. Implementation of the full Biot Savart velocity

To implement the Biot-Savart equations in the vortex filament methods we discretize the parametric curve by a large and variable number of points  $\mathbf{s}_i, i = 1 \dots N$  at initial space resolution  $\Delta\xi$ , see Fig 1. Then the velocity of the point  $\mathbf{s}$  is given by Eqs. (10a) and desingularized according to Schwarz [18]:

$$\begin{aligned} \mathbf{V}_{\text{si}}(\mathbf{s}) = & \beta_{\text{VFM}} \mathbf{s}' \times \mathbf{s}'' + \frac{\kappa}{4\pi} \int_{\mathcal{C}} \frac{(\mathbf{s}_1 - \mathbf{s}) \times d\mathbf{s}_1}{|\mathbf{s}_1 - \mathbf{s}|^3}, \quad (12) \\ \beta_{\text{VFM}} = & \frac{\kappa}{4\pi} \ln \left[ \frac{2\sqrt{l_+ l_-}}{e^{1/4} a_0} \right]. \end{aligned}$$

The integral accounts for the influence of the whole vortex configuration  $\mathcal{C}$ , excluding the segments adjacent to  $\mathbf{s}$ . Here  $\mathbf{s}_1$  is a the point on the filament. The contribution of the line elements adjacent to  $\mathbf{s}$  is accounted for by the local term  $\beta_{\text{VFM}} \mathbf{s}' \times \mathbf{s}''$ . Here  $l_{\pm}$  are the lengths of two line elements connected to  $\mathbf{s}$ ,  $e = 2.71\dots$  is the base of natural logarithm and  $e^{1/4}$  corresponds to the arbitrary chosen Rankine model of the vortex core [48].

The distances between adjacent line points change during evolution. The space resolution affects the accuracy of the derivatives  $\mathbf{s}'$  and  $\mathbf{s}''$ [45]. To keep  $l_{\pm}$  of the same order of magnitude we remove a line point whenever two

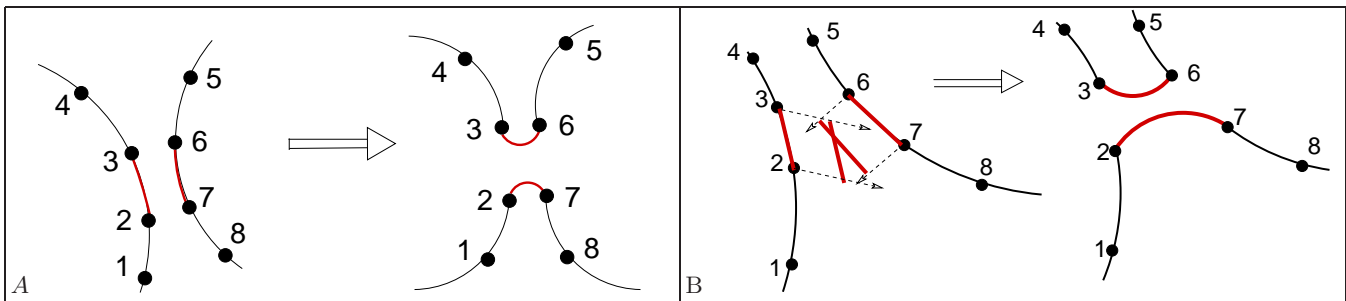


FIG. 2: Topology change for the geometric (GC) and geometric-energetic reconnection criteria (GEC) (Panel A) and “dynamical reconnection criterion (DC) (Panel B). The GC requires  $l_{2,7} < \Delta\xi$  regardless the value of other distances, while GEC requires  $l_{2,7} < \Delta\xi$  and, in addition,  $l_{2,3} + l_{6,7} > l_{2,7} + l_{3,6}$ . The DC requires that the segments (2,3) and (6,7), moving with constant speed, will cross in space during next time step.

points come closer than  $\Delta\xi_{\min}$  and add a point by a circular interpolation [19] if the distance between two adjacent points become larger than  $\Delta\xi_{\max}$ . Here  $\xi_{\min}$  and  $\xi_{\max}$  are the chosen smallest and largest interpoint distances.

## B. Criteria of vortex reconnection

In vortex filament methods the reconnections are introduced algorithmically. When some criterion is satisfied the vortex line topology is changed as shown in Figs. 2. These criteria are based on numerous studies of the vortex reconnections in the framework of the Biot-Savart and the Gross-Pitaevskii equations and on the resulting physical intuition.

### 1. Schwartz’s geometrical criterion in LIA

Historically the first criterion was suggested by Schwarz [18, 19] in the context of the local induction approximation. He noticed that when two vortices approach each other closer than  $2R/\Lambda$  (the distance at which the self-induced velocity, given by Eq. (11), is of the order of the non-local contribution) the vortex-vortex interaction dominates the local contribution, which in the framework of Eqs. (10a) leads to a local instability. During this process the velocity field of each vortex deforms the other in such a way that the vortices are moved toward each other and finally reconnect. Clearly, all this dynamics cannot be captured by the local induction approximation, which completely ignores the inter-vortex interactions. Thus Schwarz suggested a criterion that can be referred to as a “geometric criterion” for the local induction approximation, or LIA-GC: the vortices are reconnected when they approach each other closer than the minimal distance  $\delta_{\text{LIA-GC}}$

$$\delta < \delta_{\text{LIA-GC}} \equiv 2R/\Lambda, \quad (13)$$

i.e. the distance at which the nonlocal interactions exceed the local interactions.

### 2. Other geometric criteria for full Biot-Savart equations

In the framework of Biot-Savart equations the LIA-GC criterion leads to many spurious reconnections. On the other hand, conceptually these equations provide an adequate description of the vortex dynamics in the reconnection processes up to the stage when  $\delta \sim a_0$ . Therefore the vortex filament method with the full Biot-Savart equations describes the vortex line motion for distances limited by its resolution  $\delta > \Delta\xi$ .

During the last decade several reconnection criteria were proposed, in which the closeness of the reconnecting points were related to the space resolution with or without additional physical requirement. Similar to [41] we consider here two such criteria.

A natural extension of LIA-GC (13) was suggested in Refs. [22, 37]:

$$\delta < \delta_{\text{BSE-GC}} \simeq \Delta\xi, \quad (14)$$

By analogy with LIA-GC criterion (13) we call this rule “BSE-geometrical criterion” (BSE-GC), see Fig. 2 A.

Unfortunately the simple BSE-GC (14) ignores energy dissipation during reconnection events, e.g. due to phonon emission. Since the vortex length approximates the kinetic energy of the tangle, it cannot increase during reconnections. A more restrictive criterion was suggested in Ref. [28], requiring a total vortex line length reduction in addition to the geometrical proximity Eq. (14). We will refer to this criterion as to BSE “geometric-energetic” criterion (BSE-GEC). In the present work we deal only with full Biot-Savart simulations and therefore we skip hereafter the notation “BSE-” from the reconnection names and abbreviate them shortly as GC and GEC (or G-criterion and GE-criterion).

### 3. Dynamical criterion

The authors of Refs. [38–40] approached the problem of reconnection criterion completely differently, by considering the dynamics of vortex line points. Their approach



$T, \text{K}$	1.3	1.6	1.9
$\alpha$	0.036	0.098	0.210
$\alpha'$	0.014	0.016	0.0009
$\rho_n/\rho$	0.045	0.162	0.420
$\alpha\rho/\rho_n$	0.8	0.6	0.5
$\tilde{\Lambda} \equiv \Lambda/(4\pi)$	1.05	1.03	1.02

TABLE I: Friction parameters  $\alpha$  and  $\alpha'$  used in simulations, relative density of the normal component [49], combination  $\alpha\rho/\rho_n$  [which weakly depends temperature and is responsible for the mutual friction density in Eq. (8d)] and LIA parameter  $\tilde{\Lambda}$  calculated for  $c = 1$ .

is equally applicable to the local induction approximation as well as the Biot-Davart dynamics. Under the assumption that both ends of a line segment are moving at the same velocity during a time step, the reconnection is carried out if the reconnecting line segments cross in space during the next time step. We will refer to this criterion as the "dynamical" criterion (DC or D-criterion). Note that unlike GC and GEC, the DC involves reconnecting segments and not points. The assumption of the same velocity of the two ends of a segment implies sufficiently high space resolution (small values of  $\Delta\xi$ ) -see Fig. 2 B.

To find whether the line segments will meet during the next time step, the set of equations

$$\begin{aligned} \mathbf{s}_i + V(\mathbf{s}_i)\tau + (\mathbf{s}_{i+1} - \mathbf{s}_i)\theta = \\ \mathbf{s}_j + V(\mathbf{s}_j)\tau + (\mathbf{s}_{j+1} - \mathbf{s}_j)\phi \end{aligned} \quad (15)$$

is solved for  $0 \leq \theta \leq 1$ ;  $0 \leq \phi \leq 1$ ;  $0 \leq \tau \leq \Delta t$ . If such a solution is found, the segments will collide. Here  $\mathbf{s}_i = (x_i, y_i, z_i)$ ,  $\mathbf{s}_{i+1} = (x_{i+1}, y_{i+1}, z_{i+1})$  and  $\mathbf{s}_j = (x_j, y_j, z_j)$ ,  $\mathbf{s}_{j+1} = (x_{j+1}, y_{j+1}, z_{j+1})$  (in Cartesian coordinates) denote the first and the second reconnecting pairs of points and  $\Delta t$  is the time step. The velocities  $V(\mathbf{s}_i)$  and  $V(\mathbf{s}_j)$  remain the velocities of the line points  $\mathbf{s}_i$  and  $\mathbf{s}_j$ . Alternatively, the velocities of the midpoint of the segments  $(i, i + 1)$  and  $(j, j + 1)$  may be used.

### C. Implementation Details

The simulations were carried out in the cubic box  $H = 0.1$  cm for temperatures  $T = 1.3$  K, 1.6K and 1.9K and counterflow velocities  $V_{\text{ns}}$  from 0.3 cm/s to 1.2 cm/s. The parameters  $\alpha$  and  $\alpha'$  are given in Table I. The initial condition consisted of 20 circular rings of radius  $R_0 = 9 \times 10^{-3}$  cm oriented such that the total momentum of the system vanished. The radius of the rings was chosen to exceed the critical radius of the surviving loop[18, 20]  $R_{\text{cr}} \approx 3 \times 10^{-3}$  for the weakest thermal flow ( $T = 1.3\text{K}$ ,  $V_{\text{ns}} = 0.3\text{cm/s}$ ).

The initial space resolution  $\Delta\xi = 8 \times 10^{-4}\text{cm}$  for D-criterion and  $1.6 \times 10^{-3}\text{cm}$  for GC and GEC was used. At these values the results were insensitive to the resolution as was verified by simulations with larger and

smaller values of  $\Delta\xi$ . As it was mentioned above, the line points were removed or added during evolution to keep  $\Delta\xi/1.8 \leq l_{\pm} \leq 1.8\Delta\xi$ .

We use the 4-th order Runge Kutta method for the time marching with the time step related by the stability condition to the line resolution. For simulations with GC and GEC  $\Delta t = 3.8 \times 10^{-4}\text{s}$ , while for DC  $\Delta t = 9.5 \times 10^{-5}\text{s}$  was used. The time evolution was followed for 150 seconds for GC and GEC and for 75 seconds for DC.

The directionality of the vortex lines is conserved during the reconnection procedure. The candidate points for reconnections are sought within  $1.1\Delta\xi$  distance for GC and GEC and within the distance defined by a maximum velocity in the tangle at the reconnection time  $2\Delta t V_{\text{max}}$  for DC. Note that in [41] the candidate pairs for similar criterion were sought within distance  $\Delta\xi$ .

Similar to [22], we remove the small loops and loop fragments with three or less line segments that are expected to disappear due to the mutual friction. The maximum length of the removed loops is  $8.6 \times 10^{-3}$  cm for DC and  $1.7 \times 10^{-2}$  cm for GC and GEC, which is smaller than the length of the loop of the critical size  $1.88 \times 10^{-2}$  cm. This procedure was applied in all simulations.

An additional requirement that the angle between reconnecting segments is at least 10 degrees ( $\cos(\mathbf{s}_i, \mathbf{s}_j) < 0.9848$ ), applied to GEC, was introduced similar to [41]. We performed simulations without this additional requirement as well and did not find any difference in the results.

In BSE simulations, the main computational domain is surrounded by 26 replicas that take care of the boundary conditions. We have verified that the influence of the replica domains touching the cube edges and corners is negligible. The influence of the replica domains bordering the faces of the main domain was studied and discussed below. All results below are calculated using only the main computation domain.

At each time step we propagate the line points, adjust the space resolution, perform the reconnections, remove small loops and then adjust the resolution again. Unlike [41] we reconnect all pairs of points and segments that satisfy the reconnection criterion, and not just the closest ones. This may lead to slightly larger number of reconnection than in [41].

## III. DYNAMICS OF THE VORTEX TANGLE

### A. Evolution of the tangle toward steady state

A typical time evolution of the vortex tangle is shown in Fig. 3. Panel A illustrates that the steady state is independent of the initial conditions: the evolution at  $T = 1.6$  K and  $V_{\text{ns}} = 1$  cm/s, started from the 20-ring configuration (blue solid line) as well as from the steady state configurations for  $T = 1.3\text{K}$  and  $T = 1.9\text{K}$ , (green dashed and red dot-dashed lines, respectively) all give the

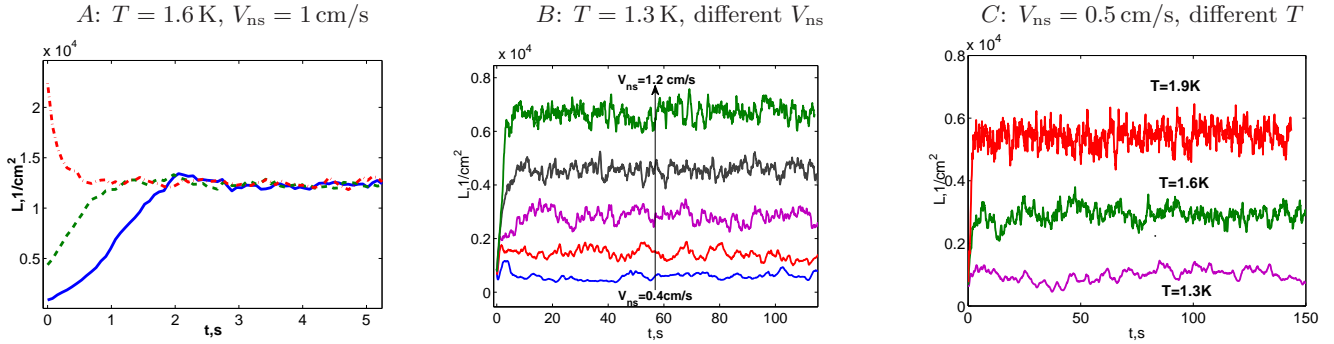


FIG. 3: Color online. Panel A: Transient regime (with GEC) started from 20-ring configuration (blue solid line), from the steady state configuration obtained at  $T = 1.3 \text{ K}$  (green dashed line) and from the steady state configuration obtained at  $T = 1.9 \text{ K}$  (red dot-dashed line). Panel B: VLD evolution  $T = 1.3 \text{ K}$  for counterflow velocities 0.4, 0.6, 0.8, 1.0 and 1.2 cm/s (from bottom to top). Panel C: VLD evolution for different temperatures and  $V_{\text{ns}} = 0.5 \text{ cm/s}$ .

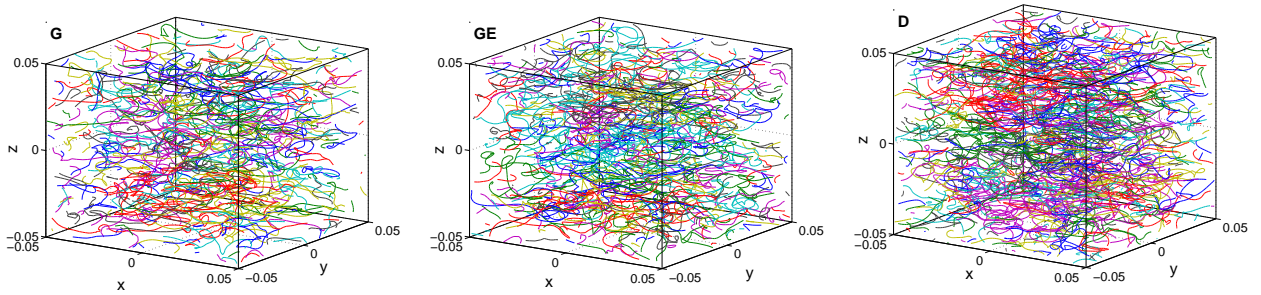


FIG. 4: Color online. Typical tangle configurations for different reconnection criteria at  $T = 1.9 \text{ K}$  and  $V_{\text{ns}} = 1 \text{ cm/s}$ .

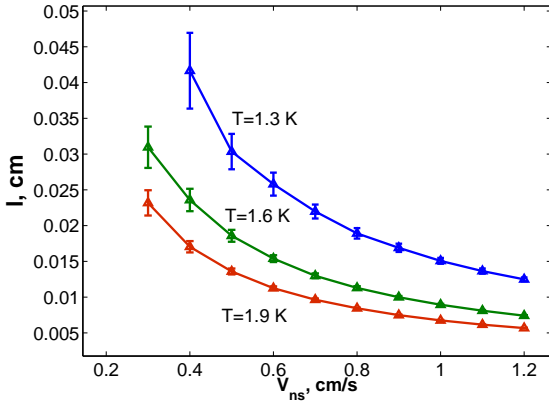


FIG. 5: Color online. The intervortex distance  $l = \mathcal{L}^{-1/2}$  as a function of  $V_{\text{ns}}$  for different temperatures. (with GEC).

same steady state vortex line density. This (expected) result allows us to perform all the simulations starting from the same simple 20-ring configuration.

As one sees in Fig. 3A, the transient time  $\tau_{\text{tr}}$  it took for the initial configuration to reach the steady state is the shortest for the most dense initial configuration (steady state at  $T = 1.9 \text{ K}$  – red dashed line) and the longest for the most sparse one (20-rings – blue solid line). This can

be easily rationalized by a dimensional reasoning according to which

$$\tau_{\text{tr}} \sim 1/(\kappa \mathcal{L}) = \ell^2/\kappa. \quad (16)$$

This dependence also agrees with our observations that  $\tau_{\text{tr}}$  is longer for low temperatures (for which the resulting  $\mathcal{L}$  is smaller), and shorter for large  $T$ , at which the tangle is more dense. For moderate values of  $\mathcal{L} \simeq 3 \cdot 10^3 \text{ cm}^{-2}$  the estimate (16) gives  $\tau_{\text{tr}} \sim 0.3 \text{ s}$ . This is slightly shorter than the values observed numerically.

The values of  $\tau_{\text{tr}}$ , deduced from Fig. 3A, agree surprisingly well with the experimental results of Vinen [10] (Fig. 2, panel d) for  $T = 1.6 \text{ K}$ . At this temperature the transient time decreases continuously with the increasing amount of initially present turbulence. When helium was not excited initially, the time to reach the steady state was about 1.9 sec. It decreased to about 1 sec for moderately excited and to less than 0.5 sec for strongly excited helium, similar to our results.

Another important characteristic of the vortex dynamics, clearly seen in Figs. 3B and 3C, is the large amplitude of fluctuations in density in the steady state, which reach up to 12% of the steady state vortex line density for weak counterflow velocities. One sees also that the mean line density increases both with  $V_{\text{ns}}$  and temperature, such that the same line density may be obtained at

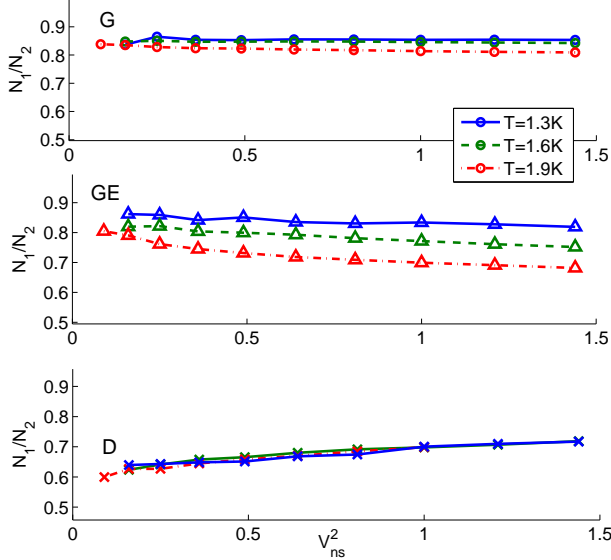


FIG. 6: Color online. Ratio of reconnection rates of two types for different conditions. Circles denote DC, up-triangles- GEC, crosses- DC. Solid lines correspond to  $T = 1.3\text{K}$ , dashed lines- to  $T = 1.6\text{K}$  and dot-dashed lines- to  $T = 1.9\text{K}$ . Lines serve to guide the eye only.

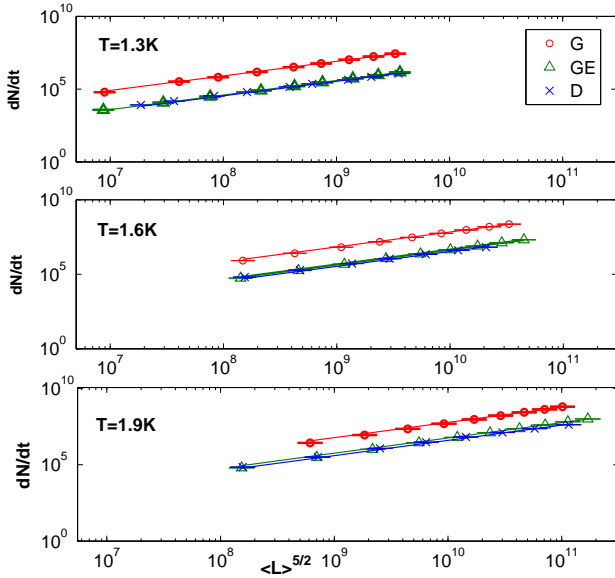


FIG. 7: Color online. The mean reconnection rate  $dN_r/dt$  as a function of  $\mathcal{L}^{5/2}$ . The symbols with errorbars are data, the lines are linear fit according to Eq. (3) (the fit passes through  $\mathcal{L}^{5/2} = 0$ ).

lower temperatures and stronger counterflow velocity or at higher  $T$  and smaller  $V_{\text{ns}}$ .

## B. Tangle visualization and intervortex distance

The typical dense steady state tangles obtained with different reconnection criteria are shown in Fig. 4 for  $T = 1.9\text{K}$  and  $V_{\text{ns}} = 1\text{ cm/s}$ . At these parameters the difference in density is visible to the naked eye: the most dense tangle is obtained with DC and the most sparse with GC. An important characteristic of the developed tangle is the intervortex distance  $\ell$  that quantifies the typical distance between the vortex lines. As seen from Fig. 5 the vortex lines come closer with increasing both counterflow velocity and temperature and  $\ell$  becomes comparable with the space resolution  $\Delta\xi$  at  $T = 1.9\text{K}$  and the largest  $V_{\text{ns}}$  used in our simulations.

## C. Reconnection dynamics

As said above, periodic boundary conditions allow only two types of reconnections: the merging of two loops into one ( $2 \rightarrow 1$ ) and one loop splitting into two ( $1 \rightarrow 2$ ). We denote below the reconnection rate per unit volume of the first type as  $N_1$  and of the second type as  $N_2$  and plot the ratio  $N_1/N_2$  as a function of  $V_{\text{ns}}^2$  in Figs. 6 for different conditions. The reconnections leading to splitting one loop into two are more frequent in all cases. For GC the ratio is almost independent of  $V_{\text{ns}}$  and the merging of loops is even less frequent at  $T = 1.9\text{K}$ . For DC the ratio is temperature independent, but the first type of reconnection becomes more frequent with increasing  $V_{\text{ns}}$ . For GEC the loops merging becomes less frequent with increasing both the temperature and the counterflow velocity. On the average only about 35 – 45% of reconnections lead to loops merging.

In Figs. 7 we show the mean reconnection rate  $dN_r/dt$  as a function of  $\mathcal{L}^{5/2}$ . One sees that the linear relation (3) is well obeyed throughout the parameter range and for all three criteria of reconnections. The values of the coefficient  $c_r$  are given in Table II. Note that for all temperatures the reconnection rate for GC is several times higher than for GEC and DC, which are close to each other and their scaling coefficients fall within the range  $0.1 < c_r < 0.5$ , as predicted by Nemirovskii [43]. The much larger number of reconnections for GC is in agreement with the results of Baggaley [41] who found that the time between reconnections for this criterion was much shorter than for GEC. We conclude that geometric-energetic and dynamic criteria give reliable values of the reconnection rates, while pure geometric criterion overestimates it by an order of magnitude.

Previously the scaling coefficient  $c_r$  was calculated in [39, 40] using DC within the local induction approximation. They found  $c_r = 2.47$  for  $T = 1.6\text{K}$  and  $V_{\text{ns}} = 6, 8$  and  $12\text{ cm/s}$ . This is much larger than our current result. The counterflow velocity in their case was much stronger than we use and their vortex line density was also much larger. Thus the difference may stem from the usage of the local induction approximation, which is doubtful for

		T=1.3K	T=1.6K	T=1.9K
$c_r$	GC	$8.0 \pm 1.0$	$6.80 \pm 0.5$	$6.0 \pm 0.3$
	GEC	$0.39 \pm 0.05$	$0.45 \pm 0.03$	$0.57 \pm 0.03$
	DC	$0.34 \pm 0.05$	$0.34 \pm 0.03$	$0.40 \pm 0.13$

TABLE II: The reconnection rate scaling coefficient. The errorbars were calculated from standard deviations of  $dN_r/dt(t)$  and  $\mathcal{L}$ .

		T=1.3K	T=1.6K	T=1.9
$\gamma$ , s/cm <sup>2</sup>	GC	$68.6 \pm 0.1$	$105.8 \pm 0.2$	$128.6 \pm 0.7$
	GEC	$72.1 \pm 0.2$	$115.7 \pm 0.1$	$148.0 \pm 0.2$
	DC	$67.1 \pm 0.4$	$120.2 \pm 0.7$	$171.2 \pm 2.6$
$\Gamma \simeq$	GEC	0.07	0.12	0.15
$10^2 v_0$ , cm/s	GC	$3.1 \pm 0.1$	$-0.8 \pm 0.1$	$-5.4 \pm 0.3$
	GEC	$6.6 \pm 0.3$	$3.3 \pm 0.1$	$0.2 \pm 0.1$
	DC	$1.6 \pm 0.4$	$4.3 \pm 0.5$	$4.3 \pm 0.4$
$\gamma$ , Ref. [22]	GC	53.1	109.6	140.1
$\gamma$ , Ref. [41]	GC		116.9	
	GE		114.35	
	DC		112.3	
$\gamma_v$ , Eq. (18)		82	151	266
$\gamma_s$ , Eq. (19)	[19]	80	130	198

TABLE III: The values of  $\gamma$  (in s/cm<sup>2</sup>) and  $10^2 v_0$  (in cm/s) obtained from Eq. (2b) and approximate values of  $\Gamma \equiv \gamma \kappa$  for GE-criterion. The errorbars for  $\gamma$  and  $v_0$  were calculated from the standard deviation of  $\mathcal{L}$  by textbook relations [50]. The values of  $\gamma$  from numerical simulations of Refs. [22, 41], from Eq. (18) and the estimate (19) with  $c_L$  from [19] are given for comparison.

these values of  $\mathcal{L}$ .

#### IV. MEAN CHARACTERISTICS OF THE TANGLE

##### A. Vortex line density $\mathcal{L}$

###### 1. Numerical results for $\mathcal{L}$ vs. counterflow velocity

The steady state value of  $\mathcal{L}$  was obtained by averaging  $\mathcal{L}(t)$  over the plateau values for 10 – 150 s for  $T = 1.3$  K and for 5 – 150 s for  $T = 1.6$  and 1.9 K for GC and GEC and up to 75 s for DC. The error bars in the figures were calculated by the standard deviation over the same time period. In Fig. 8 we present  $\mathcal{L}$  as a function of the counterflow velocity and the fit according to Eq. (2b). Clearly the data follow this linear relation faithfully and the corresponding  $\gamma$  and  $v_0$  are given in Table III. A measurable difference between the results with only the main computational domain and with additional 6 replicas touching its faces was found only for  $T = 1.9$  K and  $V_{ns} > 0.5$  cm/s, resulting in  $\gamma = (146.2 \pm 0.2)$  s/cm<sup>2</sup> compared to

$\gamma = (148.0 \pm 0.2)$  s/cm<sup>2</sup> (for GE-criterion) for the main domain (about 1% difference). Similar corrections were obtained for the other criteria. We therefore conclude that for the parameter range used in our work it is sufficient to calculate the Biot-Savart velocities in the main domain only.

The values of  $\gamma$  which was calculated in [41] were obtained for counterflow velocities  $0.35 < V_{ns} < 0.6$  cm/s at  $T = 1.6$  K, while in [22] a similar range of  $V_{ns} < 0.6$  cm/s was used for  $T = 1.9$  K. For these parameters we found that the difference in the computed value of  $\mathcal{L}$  for different reconnection criteria was relatively small. Our simulations with wider range of counterflow velocities demonstrates that the values of  $\mathcal{L}$  for three reconnection criteria are close only for  $T = 1.3$  K, while for  $T = 1.6$  K and 1.9 K they progressively deviate from each other, leading to different values of  $\gamma$  – see Fig. 8 and Tab. III. Quantifying the spread of the values as a difference between the largest and the smallest  $\gamma$  at each temperature divided by the mean value, we get about 7% for  $T = 1.3$  K, about 13% for  $T = 1.6$  K and about 28% for  $T = 1.9$  K.

###### 2. Comparison of numerical and experimental results

In Fig. 9 we compare the values of  $\gamma$  obtained in simulations with the experimental results. This is an issue that requires careful analysis of particular experimental conditions including the dependence on the channel width, the roughness of the walls, the finite value of the temperature difference with respect to the mean temperature and problems with temperature stabilization.

Additional uncertainty arises from the fact that the thermal counterflow turbulence in square channels of width smaller than 1 mm may exist in two turbulent regimes[13]. The regime TI immediately follows the laminar state. The regime TII is found above some critical line density, usually at higher counterflow velocities. In both regimes  $\mathcal{L}^{1/2} = \gamma(V_{ns} - v_0)$  with  $\gamma$  in TII state larger than that in TI.

All these problems lead to a wide spread of experimental values of  $\gamma$  – see lines 1, 2, 3, 4 in Fig. 9.

The values of  $\gamma$  for pure superflow (thin lines with open symbols – lines 1 and 2) are significantly larger than those for counterflows in TI state (thin lines with filled symbols – lines 3 and 4). As was discussed in Ref. [17], the values of  $\gamma$  in superflows are close to the results of counterflow in TII state.

Ignoring these differences in the experimental conditions, we note that i) the spread of numerical results (ours and from Ref.[22]) is smaller than that of the experimental data; ii) the numerical results lie within the spread of experimental values of  $\gamma$ .

More experimental work is needed to better measure the values of  $\gamma$  and more numerical simulations are required to account, for example, for the boundary conditions with strong vortex pinning and laminar velocity profile of the normal components, which is not expected

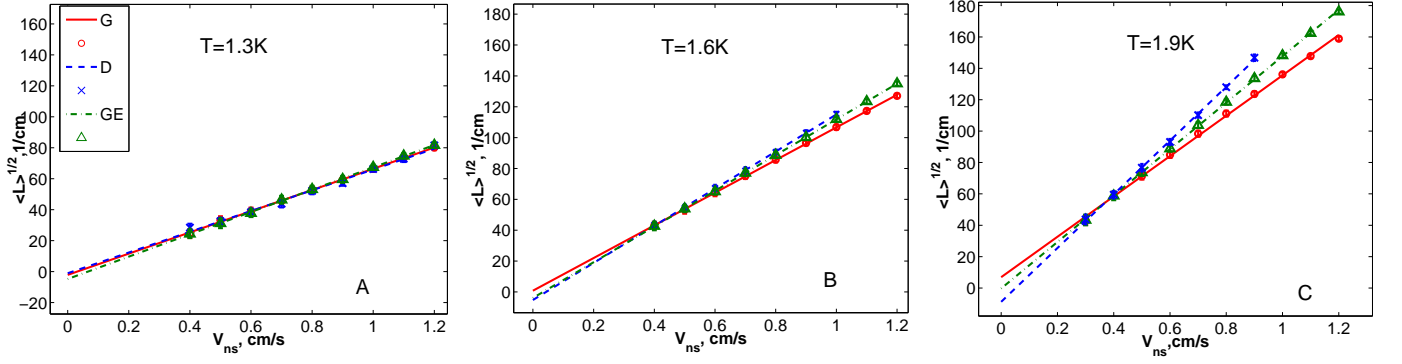


FIG. 8: Color online.  $\sqrt{\mathcal{L}}$  as a function of  $V_{ns}$  for  $T = 1.3\text{ K}$  (Panel A),  $T = 1.6\text{ K}$  (Panel B) and  $T = 1.9\text{ K}$  (Panel C). Symbols with errorbars are the numerical results, lines are fits according to Eq. (2b). Three sets of symbols and lines correspond to different reconnection criteria as shown in the legend in Panel A.

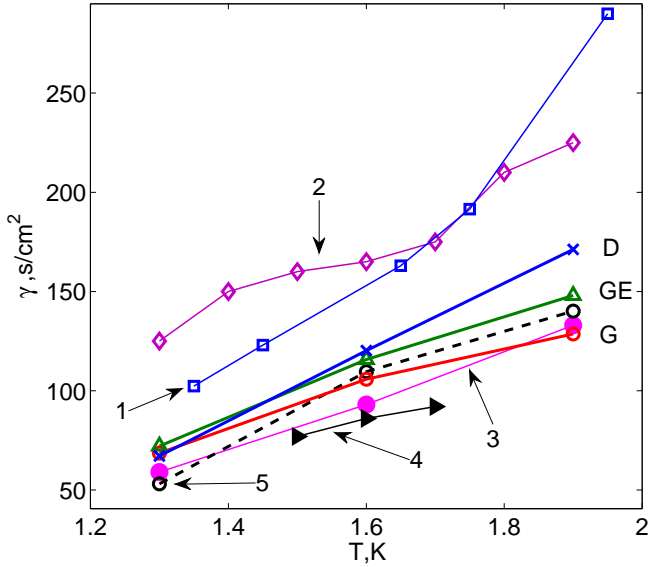


FIG. 9: (Color online). The numerical and experimental values of the parameter  $\gamma(T)$ . Thick solid lines with open symbols, marked with letters D (blue line with crosses), GE (green line with up-triangles) and G (red line with circles) are the results of our simulations with different reconnection criteria (DC, GEC and GC, respectively). Line 5, black open circles with dashed line- the simulations of Adachi et al [22], G-criterion. Thin lines with open symbols are the results of experiments in pure superflow: line 1 - Babuin et al [17] (7x7 mm channel); line 2 - Ashton et al [23], 0.13- mm diameter glass channel. Thin lines with filled symbols are the results of experiments in counterflow: line 3- Childers and Tough [12], TI state, 0.13-mm diameter glass channels, line 4- Martin and Tough [51] TI state, 1-mm diameter glass channel.

to be a constant even for pure superflow. Nevertheless, numerical and experimental results demonstrate qualitatively the same kind of behavior that allows us to hope that the main characteristics of turbulent counterflow are

adequately reflected in the numerical simulations.

### 3. Dependence of numerical results for vortex line density on reconnection criteria

As we showed above, the values of  $\gamma$  for three different reconnection criteria increasingly differ with increasing temperature. These differences may be related to larger values of  $\mathcal{L}$ , i.e. to smaller inter-vortex distance  $\ell = 1/\sqrt{\mathcal{L}}$ . A possible explanation is that the vortex filament method with any reconnection criterion deteriorates when  $\ell$  approaches the inter-point distance  $\Delta\xi$ , but the degree to which the dynamics of the tangle is affected depends on the reconnection criterion. We performed several control simulations with higher  $V_{ns}$  (not shown). Simulations at  $T = 1.3\text{ K}$  and  $V_{ns} = 2\text{ cm/s}$  resulted in  $\mathcal{L}$  similar to that for  $T = 1.9\text{ K}$  and  $V_{ns} = 0.9\text{ cm/s}$  and followed the same line as all other results for  $T = 1.3\text{ K}$ . On the other hand, at  $T = 1.9\text{ K}$  and  $V_{ns} = 2\text{ cm/s}$ ,  $\Delta\xi \approx \ell$  and the value of  $\mathcal{L}$  was strongly underestimated. In all our simulations the ratio  $\Delta\xi/\ell \leq 0.2$  and we have checked that with twice larger ratio we got practically the same results.

We should stress that the steady state value of  $\mathcal{L}$  is a result of a delicate balance of all the dynamical processes that are effected by the reconnections, explicitly and implicitly, via details of the resulting tangle characteristics. The final steady state value of  $\mathcal{L}$  may be counterintuitive. For instance, there exists an apparent contradiction: the only difference between GC and GEC is that in GC the reconnections increasing the length of the vortex line are allowed. Given a much larger number of reconnections in this case, one expects that the vortex line density should be larger for GC than for GEC, while in fact it is smaller. To resolve this contradiction we analyzed the change in the length of the vortex tangle during transient evolution, before the steady state tangle was formed. It turns out that the reconnection procedure for GC produce a large number of small loops and loops fragments with a

number of segments not exceeding three. The number of these small loops increases as the tangle develops. Since in our procedure such small loops are removed from the configuration only after all the reconnections were made, only truly separate loops that did not merge back into larger loops are removed. The number of such small loops in GEC is about 10 times smaller, while with DC they are hardly created at all. Removal of these small rings slows down the growth of the length of the vortex tangle, in particular for GC, and results in smaller steady state vortex line density in this case. For DC, on the other hand, no such mechanism exists and the vortex line density grows more before reaching the steady state value.

In the developed tangle the total length change due to reconnections, small loops removal and re-meshing is small compared to the total line length and in a self-consistent manner helps to maintain the density of the tangle around its steady state value. At this stage the difference between the reconnection criteria is not significant.

#### 4. Phenomenological analysis of $\gamma(T)$

The naïve dimensional estimate  $\Gamma \sim 1$  gives  $\gamma \sim 1000 \text{ s/cm}^2$ . Much better estimates were obtained by using macroscopic properties of the vortex tangle.

In 1957 Vinen [9] suggested a phenomenological evolution equation for the  $\mathcal{L}$ :

$$\frac{d\mathcal{L}(t)}{dt} = \frac{\chi_1 B \rho_n \mathcal{L}^{3/2}}{\rho} |V_{\text{ns}}| - \frac{\chi_2 \kappa \mathcal{L}^2}{2\pi}. \quad (17)$$

It includes the vortex generation and vortex decay terms on its RHS. Here  $B(T)$  is the Hall-Vinen temperature dependent dimensionless coefficient, describing the interaction between the line and the normal fluid, while  $\chi_1(T)$  and  $\chi_2(T)$  are additional dimensionless phenomenological parameters. In the steady state Eq. (17) results in the relation (2a) with

$$\gamma_v = \frac{\pi B \rho_n \chi_1}{\kappa \rho \chi_2}. \quad (18)$$

Estimates of the coefficient  $\gamma_v$  with experimental values for  $B$  (for  $V_{\text{ns}} = 1 \text{ cm/s}$ ) and  $\chi_1, \chi_2$  [9, 12, 49] are shown in Tab. III. These values are close to the experimental  $\gamma$  measured in superflow [17, 23].

Another estimate was obtained by Schwarz [19], who derived the equation of motion for the line density similar to Vinen's equation (17) from local induction approximation and balanced in the steady state tangle the mean anisotropy of the self-induced velocity  $\mathbf{s}' \times \mathbf{s}''$  in the Eq. (11) against its magnitude:

$$\gamma_s = c_L / \beta, \quad c_L \equiv I_\ell / c_2^2. \quad (19)$$

Recall that  $\beta = \kappa \tilde{\Lambda}$  and the values of  $\tilde{\Lambda}$  are very close to unity, such that  $\gamma_s \approx 10^3 c_L$ .

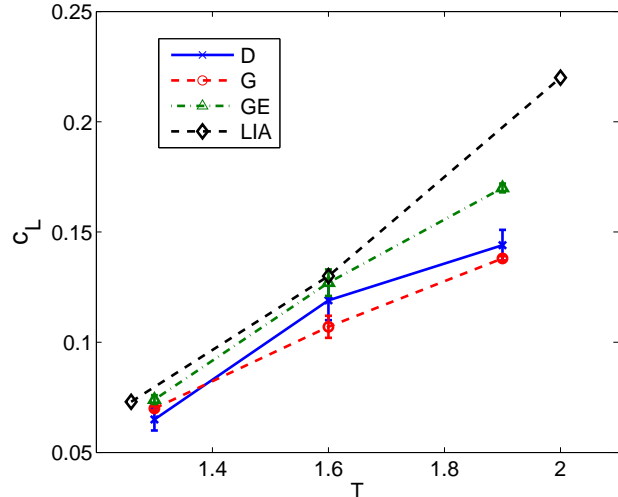


FIG. 10: Color online. The coefficient  $c_L$  found in our VFM simulations with full Biot-Savart equations for different reconnection criteria and the LIA-VFM simulations of Schwarz [19]

The parameter  $c_L$ , relating the  $V_{\text{ns}}$ -dependence of  $\mathcal{L}$  to the tangle anisotropy and RMS curvature, is one of the most important parameters of Schwarz's theory [19]. It defines, among other properties, the tangle drift velocity and the mutual friction force, discussed later in Secs. IV D and IV E. We can calculate  $c_L$ , using  $I_\ell$  and  $c_2$  given in Table IV, and see how well the theory based on the local induction approximation works for the vortex tangles, obtained with full Biot-Savart simulations.

As we discuss in Secs. IV B and IV C, the anisotropy index  $I_\ell$  is almost independent of both the temperature and the reconnection criterion, while  $c_2$  changes with  $T$  and differ for different reconnection criteria. Therefore, the  $T$ -dependence of  $c_L$  (and consequently, that of  $\gamma_s$ ) is defined by the RMS curvature scaling coefficient  $c_2$ .

In Fig. 10 we show the parameter  $c_L$  for three reconnection criteria and the results of Schwarz [19], obtained with local induction approximation simulations. The overall trend is very similar to that of  $\gamma$ , shown in Fig. 11, except that in this case it is the GE-criterion that gives the largest values and not DC, as for  $\gamma$ . As could be expected, the results for the three criteria differ most at  $T = 1.9 \text{ K}$  and the estimates for  $\gamma_s \approx 10^3 c_L$  give values slightly larger than  $\gamma$ , see Table III. The values of  $c_L$ , obtained by Schwarz from the local induction approximation simulations, are even larger. We therefore conclude that the nonlocal corrections to the line velocity affect the mean tangle properties by decreasing the vortex line density for stronger counterflow velocities.

Schwarz [19] also related the phenomenological coefficients  $\chi_1$  and  $\chi_2$  to the properties of the steady state tangle as  $\chi_1 = I_\ell, \chi_2 = 2\pi\alpha\beta I_\ell / \kappa c_L$ . Indeed, substituting these definitions to Eq. (18) and recalling that  $\alpha = B\rho_n / 2\rho$ , we find that within the local induction approximation  $\gamma_v = \gamma_s$ . However, the values of  $\gamma_s$  obtained

with Schwarz's values of  $c_L$  are smaller than  $\gamma_v$ .

Comparing Eqs. (2a) and (19) we find that both  $\Gamma$  and  $c_L/\tilde{\Lambda}$  relate the counterflow velocity to the vortex line density. Therefore we can expect that the numerical smallness of  $\Gamma \sim c_L \sim 0.1$  as well as their temperature dependence have similar origin. For  $c_L = I_\ell/c_2^2$  it is the RMS curvature scaling coefficient  $c_2$  that mostly defines the value and  $T$ -dependence. Some discrepancy in the behavior of  $c_L$  and  $\gamma$ , calculated from our tangles with different reconnection criteria suggests that there is no one-to-one correspondence between these two parameters. More than one mean property of the tangle is responsible for the value of steady state vortex line density in Biot-Savart simulations. However, for low and moderate temperatures (or low values of  $\mathcal{L}$ ), the estimates of  $\gamma$  via mean tangle properties are quite accurate.

### 5. Intercept velocity

The values of  $v_0$  found in our simulations are shown in Tab. III. The values are quite small, about (0.03 – 0.06) cm/s, but definitely nonzero within our accuracy of measurement. The values of  $v_0$  are very different for different reconnection criteria, including some negative values for GC. Therefore we tend to consider nonzero values of  $v_0$  not as a solid prediction of our simulations, but rather as an artefact stemming from the approximate character of the reconnection criteria. As for the larger values of  $v_0^{\text{exp}} \sim 0.1$  cm/s observed in experiments [17] they may be related to the strong pinning of quantized vortices on rough wall surfaces. This effect was not accounted for in our simulations. Arguments in favor of this statement may be found in Fig. 8 of Ref. [17] which shows that the experimental values of  $v_0$  monotonically decrease for wider and wider channels. Overall, we tend to think that the finiteness of the intercept velocity  $v_0$  is a finite size effect.

### B. Mean tangle anisotropy

The counterflow velocity defines the preferred direction in the tangle. The tangle anisotropy index  $I_{\parallel}$  and the ratio  $I_{\perp}/I_{\parallel}$  are shown in Fig. 11. The temperature dependence ( Fig. 11A) is consistent with the known picture [19, 22] that the tangle become more oriented in the direction perpendicular to the counterflow velocity with increasing temperature. This may be understood as an interplay of two contributions to Eq. (10b): the term proportional to  $\alpha$  is oriented in the plane perpendicular to  $V_{\text{ns}}$ , while the term proportional to  $\alpha'$  is locally parallel to the counterflow velocity and leads to isotropization of the loops orientation. The ratio  $\alpha'/\alpha$  diminishes upon increasing the temperature and so does the relative contribution of the this term, and the tangle become more oblate.

	recon. crit.	T=1.3K	T=1.6K	T=1.9K
$I_{\parallel}$ Eq.(4a)	GC	$0.73 \pm 0.03$	$0.76 \pm 0.02$	$0.80 \pm 0.01$
	GEC	$0.73 \pm 0.03$	$0.76 \pm 0.02$	$0.81 \pm 0.01$
	DC	$0.74 \pm 0.03$	$0.77 \pm 0.02$	$0.82 \pm 0.02$
$I_{\perp}/I_{\parallel}$ Eq.(4b)	GC	$0.86 \pm 0.06$	$0.81 \pm 0.04$	$0.74 \pm 0.02$
	GEC	$0.86 \pm 0.05$	$0.80 \pm 0.03$	$0.72 \pm 0.02$
	DC	$0.85 \pm 0.07$	$0.79 \pm 0.03$	$0.71 \pm 0.02$
$I_{\ell}$ Eq.(4c)	GC	$0.50 \pm 0.09$	$0.52 \pm 0.02$	$0.53 \pm 0.03$
	GEC	$0.50 \pm 0.08$	$0.53 \pm 0.03$	$0.54 \pm 0.02$
	DC	$0.51 \pm 0.09$	$0.53 \pm 0.03$	$0.52 \pm 0.02$
$I_{\parallel}$	GC [22]	0.738	0.771	0.820
$I_{\perp}/I_{\parallel}$	exp. [11]	$0.85 \pm 0.05$	$0.8 \pm 0.1$	$0.7 \pm 0.1$
$c_1$ Eq.(5c)	GC	$2.26 \pm 0.01$	$1.85 \pm 0.003$	$1.68 \pm 0.002$
	GEC	$2.09 \pm 0.01$	$1.68 \pm 0.003$	$1.48 \pm 0.001$
	DC	$2.28 \pm 0.01$	$1.64 \pm 0.003$	$1.48 \pm 0.004$
$c_2$ Eq.(5c)	GC	$2.70 \pm 0.10$	$2.19 \pm 0.05$	$1.96 \pm 0.03$
	GEC	$2.60 \pm 0.10$	$2.04 \pm 0.04$	$1.78 \pm 0.02$
	DC	$2.80 \pm 0.20$	$2.11 \pm 0.05$	$1.90 \pm 0.07$

TABLE IV: Anisotropy indices and mean curvature scaling coefficients. The values and errorbars for anisotropy indices are the time averages (same time interval as for  $\mathcal{L}$ ) and the standard deviation over the same period of time, respectively. The errorbars for  $c_1$  and  $c_2$  were calculated from standard deviations of  $|s'|$  and  $|s''|^2$ .

In our simulations, the DC systematically gives the most anisotropic tangle, while GC gives the most isotropic tangle. For all simulations  $I_{\parallel}$  is almost independent of  $V_{\text{ns}}$ , however for both GC and GEC a slight dependence on  $V_{\text{ns}}$  exceeding the error bars was observed (see Fig. 11B) for  $T = 1.6$  K ( not shown) and  $T = 1.9$  K. This is at variance with the results of [22] where no such dependence was observed ( for  $V_{\text{ns}} \leq 0.6$  cm/s), while the values of  $I_{\parallel}$  and of the ratio  $I_{\perp}/I_{\parallel}$  agree well with their results, as well as with the numerical results of Schwarz[19] and the experimental data by Wang *et al* [11].

The values in Fig. 11B are the time averaged values and the error bars are defined by the standard deviation of  $I_{\parallel}$  for  $I_{\parallel}$  and as a sum of standard deviations of  $I_{\parallel}$  and  $I_{\perp}$  for  $I_{\perp}/I_{\parallel}$  over the same time period. The values in Fig. 11A are the average values for a given temperature and the error bars are the largest error bars for  $V_{\text{ns}} \geq 0.4$  cm/s.

The anisotropy indices  $I_{\ell}$  and  $I_{\ell\perp}$  are practically independent of  $V_{\text{ns}}$  for all temperatures and all criteria.  $I_{\ell\perp}$  is close to zero in all the simulations indicating that the tangles are isotropic in the direction perpendicular to the counterflow velocity.  $I_{\ell} \approx 0.5$  and slightly increases with temperature (see Table IV). No measurable difference for different reconnection criteria was observed.

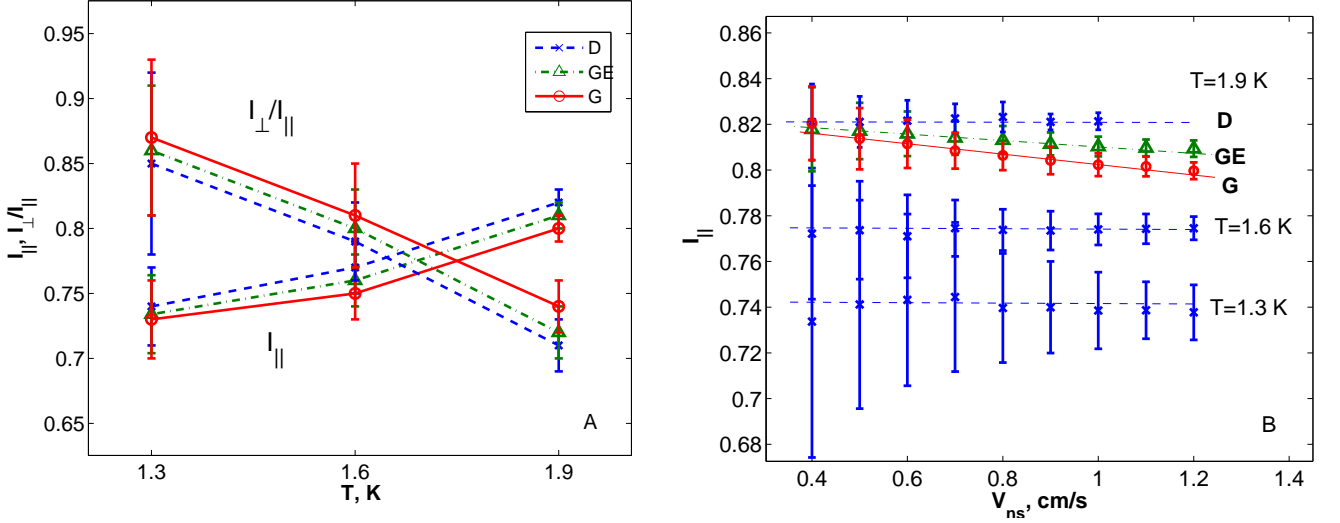


FIG. 11: Color online. Panel A: The temperature dependence of the anisotropy indices  $I_{\parallel}$  and the ratio  $I_{\perp}/I_{\parallel}$ , Eq. (4a) and (4b). Blue crosses ( $\times$ ) stand for DC, green triangles ( $\Delta$ ) for GEC and red circles for GC. Panel B: The anisotropy index  $I_{\perp}$  vs.  $V_{ns}$ . For  $T = 1.3$  K and 1.6 K only D results are shown (see text). The lines serve to guide the eye.

### C. Mean and RMS vortex-line curvature

Next important mean characteristic of the tangle is its RMS curvature  $\tilde{S} = \sqrt{\langle |s''|^2 \rangle}$ , plotted in Fig. 12A, as a function of the  $\mathcal{L}$  for different temperatures. One sees that the curvature  $\tilde{S}$  is increasing with tangle density as  $\sqrt{\mathcal{L}}$  according to Eq. (5c) with the numerical prefactor  $c_2$  that decreases as temperature grows. In other words, for the same density of the vortex lines the tangle is more curved at lower temperatures. Table IV shows that the scaling is well obeyed in simulations with all reconnection criteria and the coefficients  $c_1$  and  $c_2$  are quite close. The value of  $c_2$ , calculated at  $T = 1.9$  K with GC agrees well with the result of [52] ( $c_2 = 1.99 \pm 0.38$ ).

However some differences in the fine structure may be seen in Fig. 12B, showing the ratio of the mean radius of curvature  $R = 1/\tilde{S}$  to the intervortex distance  $\ell$ . In this way we compensate the  $\sqrt{\mathcal{L}}$  dependence of the curvature and the lines are almost flat. This ratio is distinctly different for different temperatures - the mean radius of curvature is about a third of the intervortex distance at  $T = 1.3$  K and it grows to more than a half of  $\ell$  for  $T = 1.9$  K.

The strongest change in the structure is for DC - it has the smallest  $R/\ell$  at  $T = 1.3$  K, while for  $T = 1.9$  K it appears smoother and the ratio coincides with that for GEC. For moderate and high temperatures the DC local structure appears the most sinuous.

The ratio  $R/\ell$ , shown in Fig. 12B, gives interesting *global* information about the relation between the RMS curvature and the mean intervortex distance. However it does not allow to distinguish whether the small values of  $R$  are due to dominant contributions of small loops with large curvature while the large loops are smooth, or be-

cause the large loops are fractal. To answer this and similar questions we need to have more detailed information on the vortex tangle, not only its mean characteristics.

### D. Drift velocity of the vortex tangle $V_{vt}$

In some physical problems, like the evolution of neutron-initiated micro-Big Bang in superfluid  $^3\text{He-B}$  [53], an important role is played by the drift velocity  $V_{vt}$  of the tangle with respect to the superfluid rest frame. The natural expectation is that  $V_{vt}$  is proportional to and oriented along  $V_{ns}$ . In Fig. 13A we plot  $V_{vt}$  calculated according to Eq. (7a). We see that the linear relation (7b) is well obeyed. The value of  $V_{vt}$  is fully defined by its  $z$ -component, parallel to the direction of counterflow velocity, while two other components are zero within our accuracy of measurement.

As in case of  $c_L$ , the coefficient  $C_{vt}$  may be analytically related to the structural parameters of the tangle in the Local-Induction Approximation by plugging  $ds/dt$ , Eq. (10b), with  $\mathbf{V}_{si}^{\text{LIA}}$  into (7a) and by considering different contributions to the integral [19]:

$$C_{vt}^{\text{LIA}} \approx [c_L(1 - \alpha')I_\ell + \alpha'I_{\parallel}]. \quad (20)$$

The superscript “<sup>LIA</sup>” stresses the fact that this relation is not exact, but obtained in the Local-Induction Approximation. The terms proportional to  $\alpha$  vanished in this equation by symmetry. Note that  $\alpha' = O(10^{-2})$  and therefore  $C_{vt}^{\text{LIA}} \approx c_L I_\ell$ , which is the value plotted in Fig. 31 of [19].

As we mentioned, the local contribution (11a) provides up to 90% of the total vortex velocity. Therefore we can expect that Eq. (20) will be valid with accuracy about



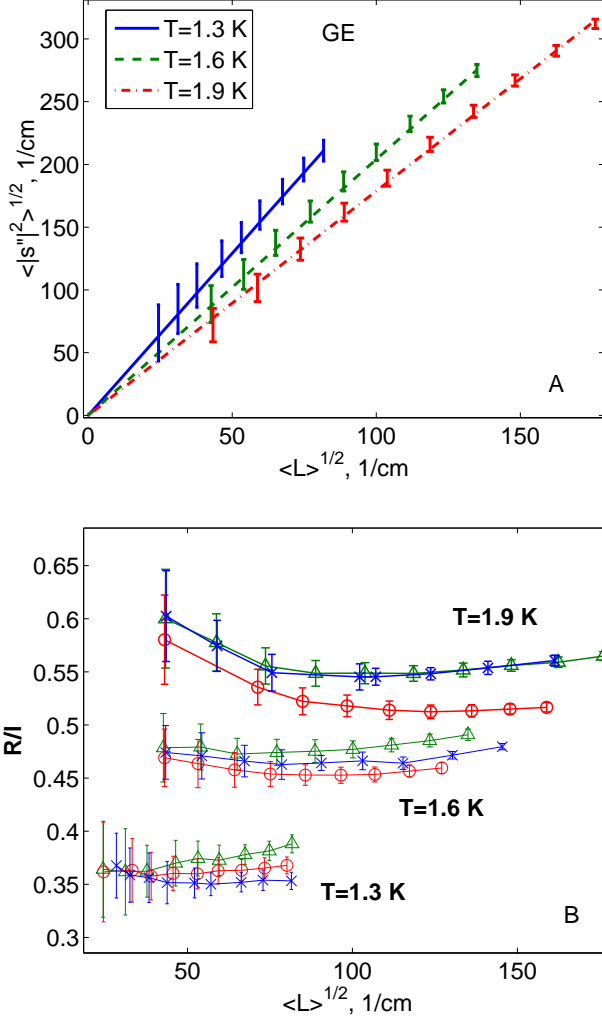


FIG. 12: Color online. Panel A: Log-log plot of mean curvature of the tangle versus the tangle density. GEC. Symbols with errorbars are data, lines are linear fit according to Eq. (5c). Panel B: Ratio of the mean radius of curvature to the intervortex distance. Red circles denote data for GC, green triangles -for GEC and blue crosses - DC. Lines serve to guide the eye only.

10%. To check this we compare in Fig. 13B the coefficients  $C_{vt}$ , obtained directly by fitting plots  $V_{vt}$  vs.  $V_{ns}$ , presented in Fig. 13A, and coefficients  $C_{vt}^{LIA}$ , given by Eq. (20), in the RHS of which we used mean vortex parameters, found in our full Biot-Savart simulations. First of all, we note that the drift coefficients for different criteria are close at  $T = 1.3$  K but differ significantly at  $T = 1.9$  K with  $C_{vt}$  for DC being almost twice larger than that for GC. Also, for DC the coefficients increase almost linearly with temperature, while for both GEC and GC the growth slows down at  $T = 1.9$  K. One sees that  $C_{vt}$  and  $C_{vt}^{LIA}$  are very close for GC and GEC, except for  $T = 1.9$  K, where  $C_{vt}$  is larger. Surprisingly,  $C_{vt}^{LIA}$  for DC is *smaller* than Biot-Savart results for all

temperatures, and in fact smaller than most of the other values. The possible reason is that the drift velocity is very sensitive to the nonlocal effects on the local tangle structure for more dense tangles (DC always gives denser tangles).

The Schwarz's  $C_{vt}^{LIA}$  found from Eq. (20) in the RHS of which the mean vortex parameters are found by simulations in the LIA [19] is very close to the GC results (both  $C_{vt}$  and  $C_{vt}^{LIA}$ ) for  $T = 1.3$  and  $1.6$  K, but is somewhat larger than  $C_{vt}$  for  $T = 1.9$  K. Comparing with Fig. 10, we see that the difference in the tangle structure ( $I_\ell$  in this case) between Biot-Savart and LIA simulations is important: for  $c_L$  the GEC results were closer to Schwarz's values. Therefore the particular closeness of different Schwarz's results to our results with different reconnection criteria is not systematic and should be taken with caution.

The main and well expected physical message is that  $C_{vt}$  is small (below upper limit of  $V_{vt}/V_{ns} = 0.2$ , suggested in [54] and in accord with results of [11]). This means that the tangle velocity is close to the superfluid velocity and its slippage is about 5% at  $T = 1.3$  K and close to 10% at  $T = 1.9$  K.

### E. Mutual friction force $F_{ns}$

The scaling of the mutual friction force  $F_{ns} \propto V_{ns}^3$  is well obeyed in all simulations with all three criteria, as we illustrate in Fig. 14A for GE-criterion. Their fit allows to find coefficients  $C_f$  plotted in Fig. 14B.

Notice that analytical expression for  $C_f$  can be found by considering different contributions to the integral  $J$  in Eq. (8a) with the only local-induction contribution to the vortex velocity  $V_{si}^{LIA}$  [19]

$$C_f^{LIA} \approx \left(\frac{c_L}{\Lambda}\right)^{2/3} (I_{||} - c_L I_\ell)^{1/3}. \quad (21)$$

Like in Eq. (20) we have added here superscript “ $LIA$ ” to stress approximated character of the relation obtained in the Local-Induction Approximation.

In Fig. 14B we compared the coefficients  $C_f$  and  $C_f^{LIA}$  for different reconnection criteria. One sees that they almost coincide for  $T = 1.3$  K. At  $T = 1.9$  K our results show significant spread of about 25% with  $C_f = 0.22$  for GC and  $0.29$  for DC. There is again a discrepancy in the behavior of  $C_f^{LIA}$ : while for GC and GEC  $C_f^{LIA} > C_f$ , especially for  $T = 1.9$  K, the LIA estimate is smaller than  $C_f$  for DC at all temperatures. The results of Schwarz[19] are larger than our values of  $C_f$  and their LIA estimates. Interestingly, here the results for DC are the closest to Schwarz's results, including linear in  $T$  behavior, albeit the largest VLD and, therefore, worst conditions for comparison with LIA results. This again confirms that the closeness of LIA and Biot-Savart results should not be taken too seriously.

The coefficient  $C_f$  is directly related by Eq. (8d) to the more experimentally used Gorter-Mellink constant  $A_{GM}$ . We plot in Fig. 15 the values of  $A_{GM}$  obtained as a fit according to Eq. (8c) as well as some experimental data. The experimentally measured values of  $A_{GM}$ , summarized by Arp [55], show significant spread. We only plot the results of Vinen[9] and Kramers et al. [56](as cited by Arp [55]). As it is clearly seen, all our values (except for GC at  $T = 1.9$  K) fall between the representative experimental results. This means that i) we get the correct order of magnitude and correct  $T$ -dependence of the Gorter-Mellink coefficient; ii) the direct comparison with particular experimental results is complicated and subject to the same difficulties as for  $\gamma$ .

### F. Mean and most probable loop lengths

The temperature and  $V_{ns}$  dependence of the mean loop length  $\bar{L}$  are shown in Fig. 16. One sees that at  $T = 1.3$  K  $\bar{L} \approx 0.33$  cm for both  $V_{ns} = 0.5$  and  $V_{ns} = 1$  cm/s but their  $T$  dependence is different:  $\bar{L}$  increases with  $T$  for  $V_{ns} = 0.5$  cm/s and decreases for  $V_{ns} = 1$  cm/s. Remarkably, the most probable loop length defined in Eq. (22) and also shown in Fig. 16, is essentially smaller, falling below 0.015 cm for the most dense tangle ( $T = 1.9$  K and  $V_{ns} = 1$  cm/s). We return to this fact below in Sec. V A.

## V. DETAILED STATISTICS OF THE VORTEX TANGLE

As we mentioned in the Introduction, the mean characteristics of the vortex tangle, studied in previous Sec. IV, provide important but very limited information on the tangle properties. Much more detailed statistical information on local tangle properties is required for better understanding of basic physics of counterflow turbulence as well as for further advance in its analytical studies. This information may be obtained from probability distribution functions of local tangle properties (like line curvature), of global vortex-loop characteristics (e.g. their lengths) and from corresponding (cross)-correlation functions (e.g. of vortex line orientations, of loop length vs. mean curvature). Bearing in mind that this information will not be available from experiments in foreseeable future, the only way to get it today is from numerical simulations. This is the motivation and the subject of present Section.

### A. Probability density function (PDF) of vortex-loop lengths

Turning to a more detailed description of the tangle structure we plot in Figs. 17 the PDF of the vortex-loop length,  $\mathcal{P}(l)$  for  $T = 1.3, 1.6, 1.9$  K and  $V_{ns} =$

0.5, 1.0 cm/s. Panel A shows that  $\mathcal{P}(l)$  is practically independent of the reconnection criterion at least for cases with moderate to large line density.

The second observation is that the core of the PDF  $\mathcal{P}(l)$  may be approximated by a simple formula

$$\mathcal{P}(l) \simeq \psi \mathcal{P}_0(l), \quad \mathcal{P}_0(l) \equiv \frac{l}{L_*^2} \exp\left(-\frac{l}{L_*}\right), \quad (22)$$

shown in Fig. 17A, left, by blue dashed line. The function  $\mathcal{P}_0(l)$  is normalized to unity:  $\int_0^\infty \mathcal{P}_0(l) dl = 1$ . The fitting parameter  $L_*$  corresponds to the maximum of the core function (22) and simultaneously to the maximum of  $\mathcal{P}(l)$ . Therefore we called it the most probable length as plotted in Fig. 16. The second fitting parameter  $\psi$  shows the fraction of loops that belong to the core and define  $L_*$ . The value of  $\psi \simeq 0.2$  for  $V_{ns} = 0.5$  cm/s and  $\psi \simeq 0.3$  for  $V_{ns} = 1$  cm/s is only very weakly dependent on  $T$ . We conclude that the majority of loops belongs to the long tail, which is clearly seen in the insets in Fig. 17. For loops lengths slightly exceeding 0.1 cm the PDF tails exhibit a power-law-like behavior over an interval of lengths about half a decade with a non-universal exponent ranging between -2 and -3 for different  $V_{ns}$  and temperatures. The mean value of the loop length  $\bar{L}$  is determined by the tails and, as we have shown in Fig. 16, is much larger than  $L_*$ .

Panels B and C of Figs. 17 show how  $\mathcal{P}(l)$  varies with temperature and  $V_{ns}$ . As we know, with increasing  $T$  and  $V_{ns}$  the VLD increases, the intervortex distance becomes smaller and the reconnection rate increases. All that shifts the PDF  $\mathcal{P}(l)$  toward shorter loops. For the least dense case ( $T = 1.3$  K and  $V_{ns} = 0.5$  cm/s) the PDF looks very indented, probably because of the lack of statistics.

### B. PDF of the line-curvature

The next object of interest is the PDF of local curvatures  $\mathcal{P}(|s''|)$ , shown in Fig. 18 for  $T = 1.3, 1.6, 1.9$  K and  $V_{ns} = 1$  cm/s. These PDFs linearly vanish for  $|s''| < \tilde{S}$  and exponentially vanish for  $|s''| > \tilde{S}$ . We suggest an interpolation formula between these two asymptotes, which is very similar to Eq. (22):

$$\mathcal{P}(|s''|) \simeq \frac{6|s''|}{\tilde{S}^2} \exp\left(-\frac{\sqrt{6}|s''|}{\tilde{S}}\right). \quad (23)$$

Notice that Eq. (23) has no fitting parameters, it just involves the RMS curvature  $\tilde{S}$ . As one sees in inset in Fig. 18, this equation describes reasonably well the entire form of  $\mathcal{P}(|s''|)$ . Accepting Eq. (23) we can find the ratio  $\bar{S}/\tilde{S} = \sqrt{2/3}$ . Correspondingly, the ratio  $c_1/c_2$  defined by Eqs. (5c) is also  $\sqrt{2/3}$ . This prediction agrees well with our numerical results for  $c_1$  and  $c_2$  given in Tab. IV. For example, for GEC the ratio  $\sqrt{3}c_1/\sqrt{2}c_2$  is equal to

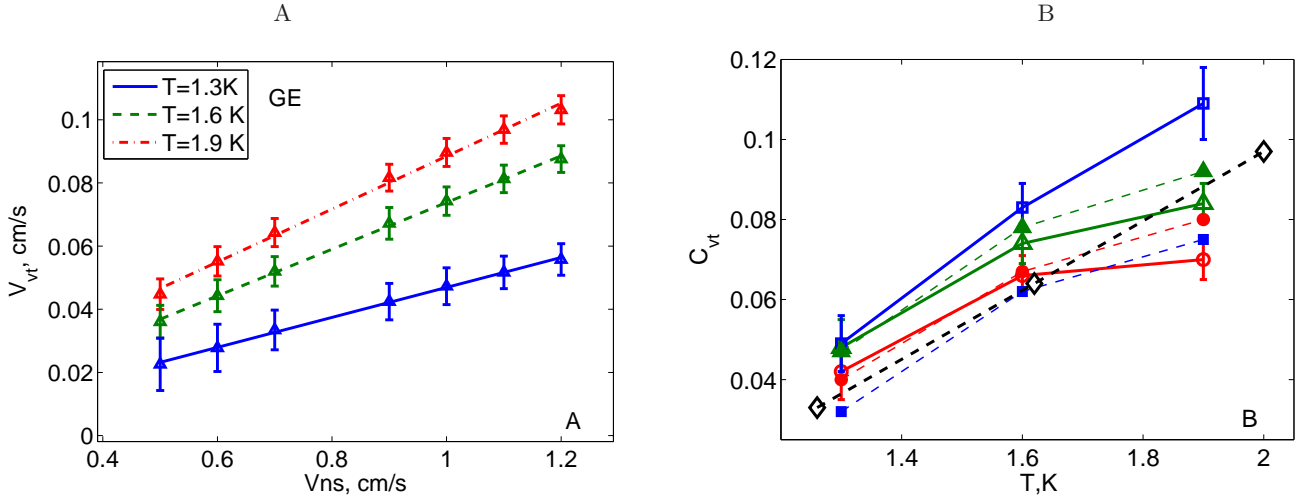


FIG. 13: Color online. Panel A: Drift velocity vs  $V_{ns}$  for three temperatures. The symbols with errorbars are data, the lines are the fit according to Eq. (7b). GE-criterion. Panel B: The drift velocity coefficient  $C_{vt}$  as a function of temperature for different reconnection criteria and their LIA estimates Eq. (20). Thick solid lines with open symbols -  $C_{vt}$  obtained by fit Eq. (7b) (red circles - GC, green triangles - GEC, blue squares - DC). Thin dashed lines with filled symbols are the LIA estimates  $C_{vt}^{LIA}$  Eq. (20) (the symbols and colors are the same as for  $C_{vt}$ ). The thick dashed line with open diamonds - the results of Schwarz[19].

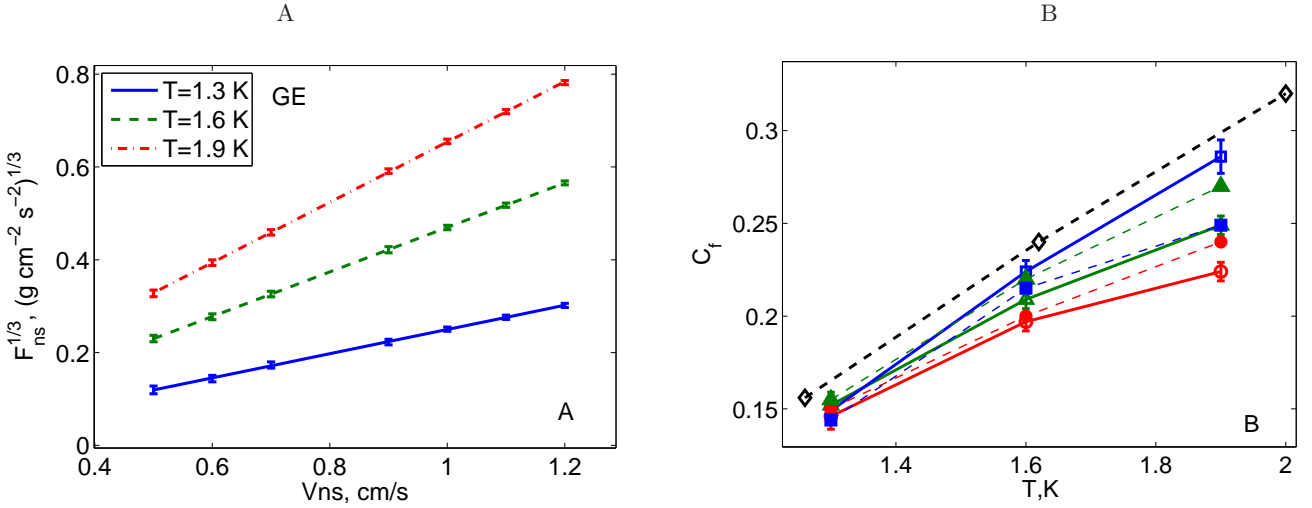


FIG. 14: Color online. Panel A: The friction force density (8a) vs counterflow velocity  $V_{ns}$ . The symbols with errorbars are data, the lines are fit according to Eq. (8b). GE-criterion. Panel B: The friction force coefficients  $C_f$  as a function of temperature for different reconnection criteria and their LIA estimates. Thick solid lines with open symbols -  $C_f$  obtained by fit according Eq. (8b) (red circles - GC, green triangles - GEC, blue squares - DC). Thin dashed lines with filled symbols are the LIA estimates  $C_{vt}^{LIA}$  Eq. (21) (the symbols and colors are the same as for  $C_f$ ). The thick dashed line with open diamonds - the results of Schwarz[19].

0.985, 1.009 and 1.018 (instead of the predicted value of unity) for  $T = 1.3$ , 1.6 and 1.9 K, respectively.

This equation also allows us to find the most probable curvature  $S_* \simeq \tilde{S}/\sqrt{6} \simeq \bar{S}/2$ . All three characteristic curvatures are determined by the exponential PDF (23) and therefore they are of the same order of magnitude. This is different from the characteristic loop lengths, where  $L_*$  is determined by the exponential core of the PDF (22), while  $\bar{L} \gg L_*$  is determined by the long

power-law tail of the PDF.

### C. Correlation between loop length $l_j$ and RMS of the loop curvature $\tilde{s}'_j$

Knowing the PDFs Eq. (22) and Eq. (23) of the loop length and line curvature separately we now come to the next question: “How are these objects correlated?” In

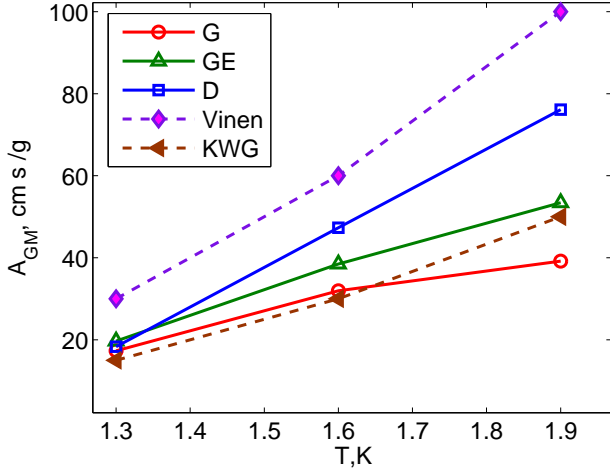


FIG. 15: Color online. The Gorter-Mellink coefficients  $A_{GM}$  as a function of temperature for different reconnection criteria. Solid lines with open symbols -  $A_{GM}$  obtained by fit according to Eq. (8c). The dashed lines with filled symbols are the experimental results of Vinen [9] and Kramers, Wiarda, and van Groenou [56].

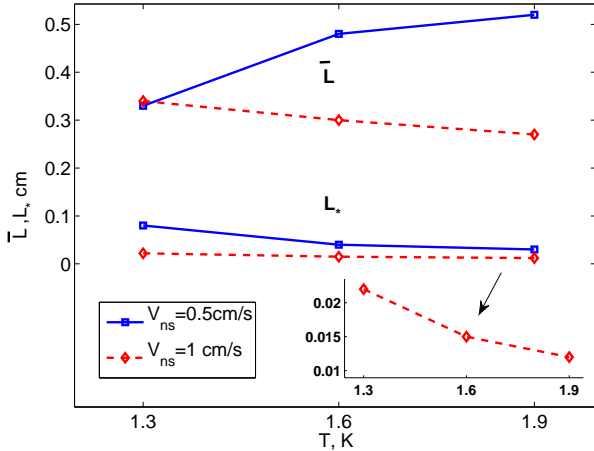


FIG. 16: Color online. Comparison of the mean loop length  $\bar{L} \sim (0.3 \div 0.5)$  cm and the most probable loop length  $L_* \sim (0.08 \div 0.01)$  cm at different temperatures and values of  $V_{ns}$ . Inset shows details of  $L_*$  for  $V_{ns} = 1$  cm/s. GEC.

particular, do all loops (long and short) have more-or-less the same RMS and mean curvatures  $\tilde{s}_j''$  and  $\bar{s}_j''$  [defined by Eqs. (6)] or do short loops have larger values of  $\tilde{s}_j''$ ? To resolve this question we plot numerous  $(\tilde{s}_j'', l_j)$ -points belonging to all loops in the statistical set of the tangle configurations, computed for particular  $T$  and  $V_{ns}$ . These points form a  $(\tilde{s}_j'' - l_j)$ -diagram shown in Fig. 19 for  $T = 1.3$  and  $1.9$  K with  $V_{ns} = 1$  cm/s.

The majority of points are located to the left of  $l_j = 0.1$  cm according to the PDFs  $\mathcal{P}(l_j)$  shown in Figs. 17.

Next, for small  $l_j$  below  $0.1$  cm one sees a sharp boundary that restricts from below available  $S_j$  at given  $l_j$ . This boundary corresponds to the minimal possible RMS loop curvature  $\tilde{s}_j'' = 2\pi/l_j$ , realized for ideal circle of radius  $1/\tilde{s}_j''$  with  $l_j = 2\pi/\tilde{s}_j''$ . Some points below this line for small  $l_j$  are the result of the finite space resolution in the continuous vortex-line presentation via a discrete set of points: the smallest loops, displayed in Fig. 19 are parameterized by only three points. Long loops have curvatures well concentrated around the conditional (with fixed  $l$ ) RMS value

$$\tilde{S}(l) = \langle \tilde{s}_j'' \rangle_{l_j=l}, \quad (24)$$

shown in Fig. 19 by blue lines (upper line for  $T = 1.9$  K and by the lower line for  $T = 1.3$  K). One sees that  $\tilde{S}(l)$  is practically independent of  $l$  for  $l$  that exceeds substantially the intervortex distance  $\ell$ , denoted by vertical lines. This is an evidence in favor of the natural expectation that local properties of long loops are independent of their total length.

#### D. PDFs of the mean and RMS loop curvature

Full information about the statistical distribution of  $\tilde{s}_j''$  for loops with given length  $l$  can be found from the conditional PDF,  $\mathcal{P}(\tilde{s}_j'', l_j = l)$ . In particular, this PDF would describe the difference in properties of short and long loops. Nevertheless, for the beginning we will restrict ourselves by analysis of less detailed information: unconditional PDFs of the mean and the RMS loop curvature,  $\mathcal{P}(\bar{s}'')$  and  $\mathcal{P}(\tilde{s}'')$ , shown in Figs. 20, A-D. In Panels A and B we compare these PDFs for the three reconnection criteria with  $T = 1.3$  K and  $V_{ns} = 1$  cm/s. They look similarly, at least on a semi-quantitative level. Therefore to clarify how these PDFs vary with  $T$  and  $V_{ns}$  it would be sufficient to analyze the results for GEC only, as shown in Panels C and D. One sees that these PDFs agree with the fact that the mean and RMS curvatures of the tangle increase with density (or  $V_{ns}$ ) for a given temperature and are smaller for higher temperatures for the same density (Fig. 12, top).

Both PDFs,  $\mathcal{P}(\bar{s}'')$  and  $\mathcal{P}(\tilde{s}'')$ , may be roughly approximated as a narrow peak of some width  $\sigma$  which is much smaller than the position of its maximum. PDF of the mean curvature looks more regular. Its core is approximated well enough by a Gaussian

$$\mathcal{P}(\bar{s}'') \approx \frac{\psi}{\sqrt{2\pi}\sigma} \exp \left\{ -\frac{(\bar{s}'' - \bar{s}_*'')^2}{2\sigma^2} \right\}, \quad (25)$$

with three fitting parameters: the position of the maximum  $\bar{s}_*''$  (the most probable mean-loop curvature), the width  $\sigma$  and the total amount  $\psi$  of  $\bar{s}''$ , described by the core of PDF (25):  $\int \mathcal{P}(\bar{s}'') d\bar{s}'' = \psi$ . This allows us to quantify the differences between curvature distributions

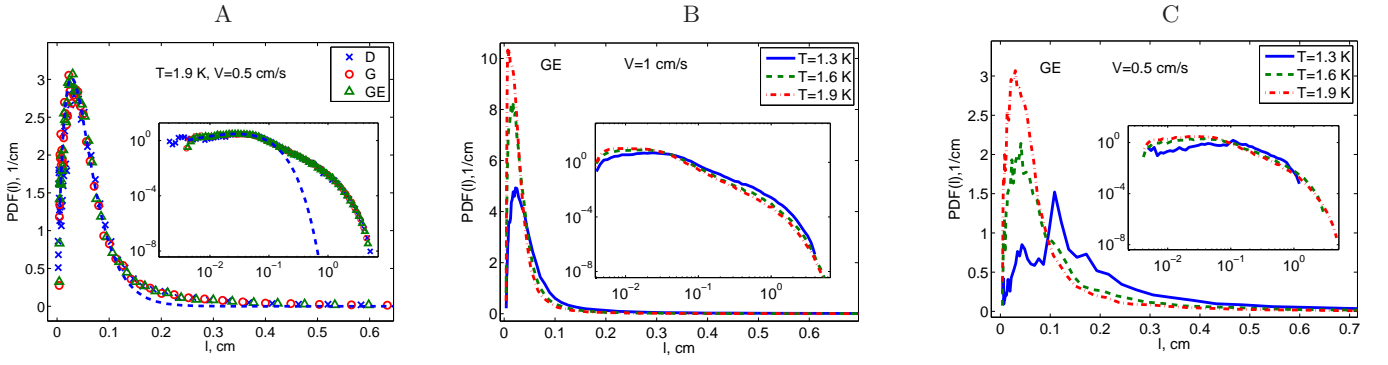


FIG. 17: Color online. PDF of the vortex-loop length  $l$ ,  $\mathcal{P}(l)$ . Panel A:  $T = 1.9$ ,  $V_{\text{ns}} = 1$  cm/s, three reconnection criteria. Blue dash lines shows exponential core of the PDF (22). Panel B:  $V_{\text{ns}} = 1$  cm/s, for  $T = 1.3, 1.6, 1.9$  K, GEC. Panel C:  $V_{\text{ns}} = 0.5$  cm/s, for  $T = 1.3, 1.6, 1.9$  K, GEC. Insets show the same PDFs in log-log scale.

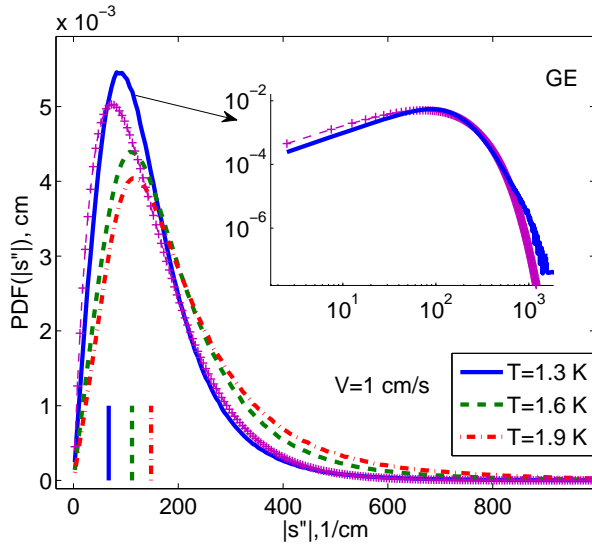


FIG. 18: Color online. PDF of local line curvature for 3 temperatures and  $V_{\text{ns}} = 1$  cm/s, GEC. Vertical lines near horizontal axis show  $1/\ell$  at given conditions. Inset: the PDF( $s$ ) for  $T = 1.3$  K (blue solid line) and the fit by Eq. (23) (purple crosses).

in a wider range of parameters. The temperature dependences of  $\overline{s''_*}$ ,  $\sigma$  and  $\psi$  are shown in Panels E and F for  $V_{\text{ns}} = 0.5$  cm/s and 1.0 cm/s, respectively. One sees that  $\psi$  is quite close to unity:  $\psi > 0.9$  at  $V_{\text{ns}} = 0.5$  cm/s and  $\psi > 0.8$  at  $V_{\text{ns}} = 1$  cm/s for all three reconnection criteria. This means that Eq. (25) describes reasonably well the entire PDF and not only its core. Therefore at our level of description the contribution of non-exponential tail can be ignored.

Notice that on a semi-quantitative level there are no differences in the values and behaviors of  $\overline{s''_*}$  and  $\sigma$  for the three reconnection criteria. Therefore in Panels E and F we presented these parameters only for GEC. In addition we show (by blue dashed lines) in the same pan-

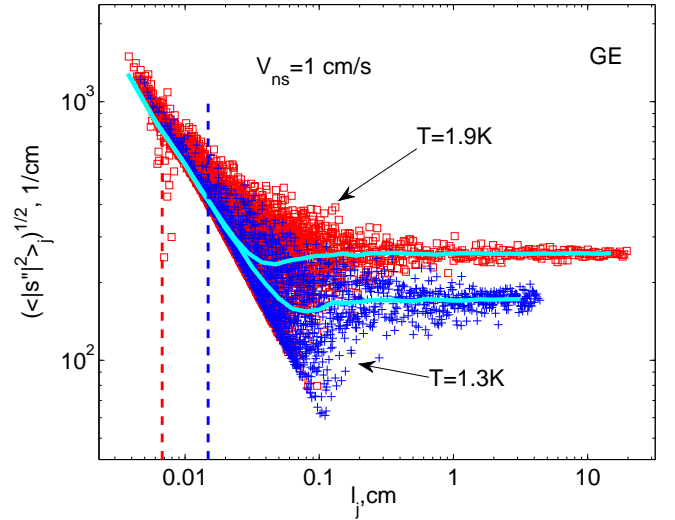


FIG. 19: Diagrams of RMS of loop-curvature  $\tilde{s''_j}$  vs. length-loop  $l_j$  for  $V_{\text{ns}} = 1$  cm/s with GEC for two temperatures. The plus sign(+) denote data for  $T = 1.3$  K, the squares - for  $T = 1.9$  K. Light blue lines correspond to the mean curvature of loops vs their length. The intervortex distances are denoted by vertical dashed lines, left - for  $T = 1.9$  K, right - for  $T = 1.3$  K.

els the overall (over the entire tangle) mean value of the curvature  $\overline{S}$  which, by definition, has to coincide with the mean (over different loops) of the mean-loop curvature:  $\overline{S} = \int s'' \mathcal{P}(s'') ds''$ . We see that the mean tangle curvature  $\overline{S}$  practically coincides with the most probable mean-loop value  $\overline{s''_*}$ . This means that the role of the PDF tail can be ignored, as we stated above on the basis that  $\psi \simeq 1$ .

The next observation is that  $\overline{s''_*}$  (and  $\overline{S}$ ) increases with temperature and counterflow velocity, i.e. with the tangle density. This agrees with the well known fact  $\overline{S} \propto \sqrt{\mathcal{L}}$ . A less expected observation is that  $\sigma$  decreases with increasing  $T$  and  $V_{\text{ns}}$ , i.e. in the denser tangle the mean-loop

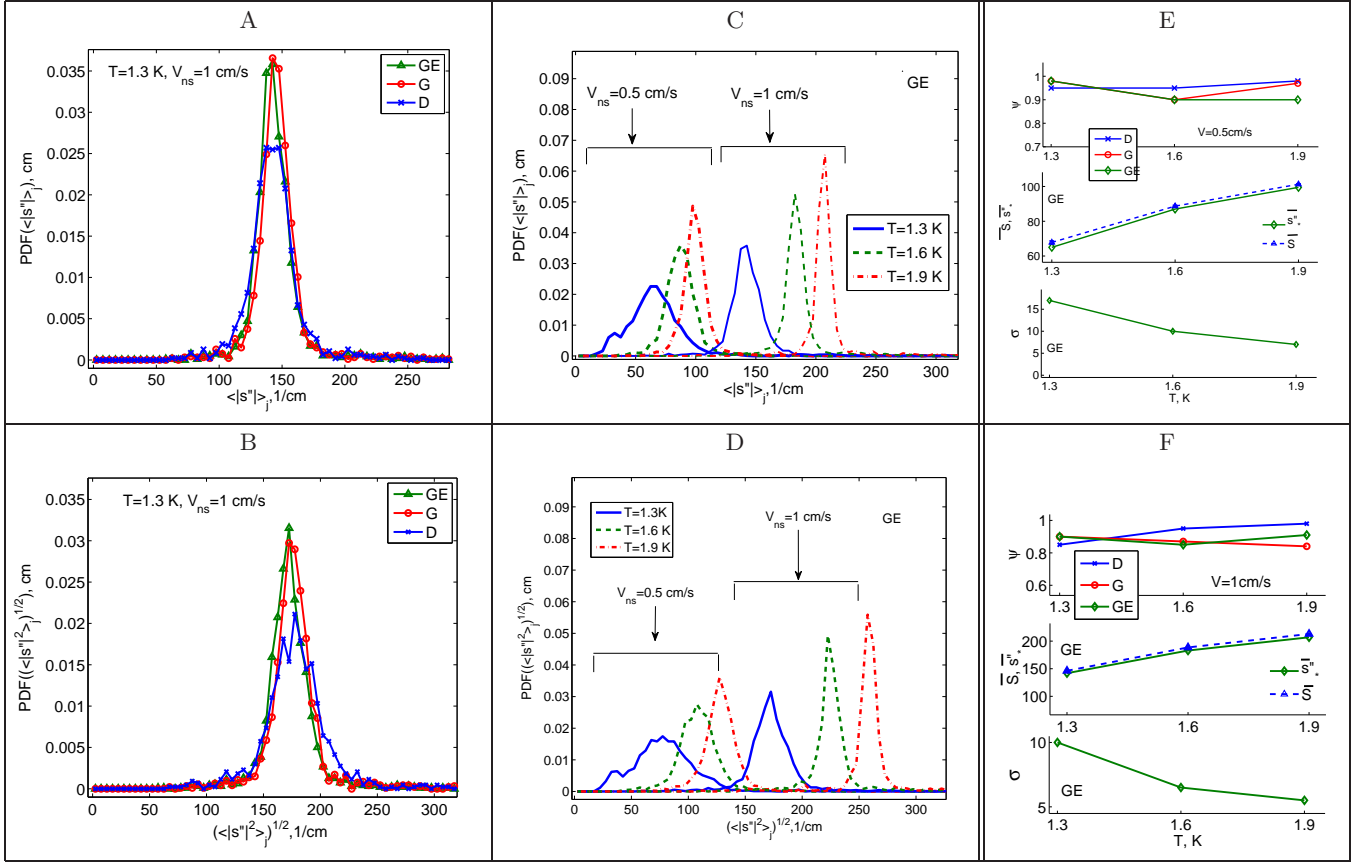


FIG. 20: Color online. Comparison of PDFs of the mean (Panel A) and RMS (Panel B) loop curvature for three reconnection criteria ( $T = 1.3$  K and  $V_{ns} = 1$  cm/s). The lines serve to guide the eye only. Temperature and  $V_{ns}$  dependence of the PDF of the mean (Panel C) and RMS (Panel D) loop curvature (for GEC). Parameters of the Gaussian fit Eq. (25) for the PDF of the mean curvature are shown in Panels E for ( $V_{ns} = 0.5$  cm/s) and F for ( $V_{ns} = 1$  cm/s).

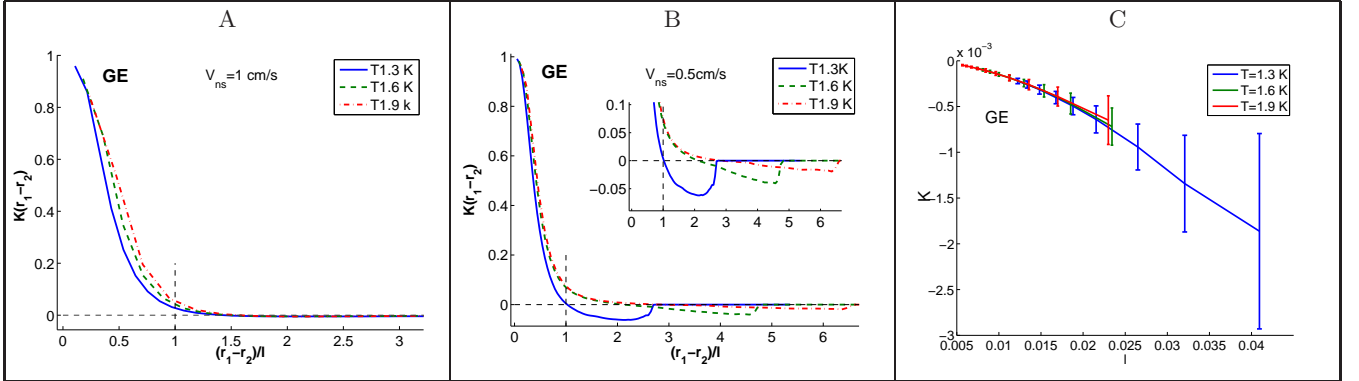


FIG. 21: Color online. Panels A and B: The orientation correlation function for different temperatures and two counterflow velocities. Inset: details of long distance tail. The distance is measured in units of intervortex distance. Panel C: The mean polarization of the tangle as a function of the intervortex distance. GEC .

curvatures are less spread around their mean (or most probable) value.

### E. Autocorrelation of the vortex orientation

It was recognized by Schwarz [47] that the structure of the vortex lines is reminiscent of random walks. As the vortex segments get further apart, their relative orientation becomes more random. To find out at which dis-

tances the correlation between the segment orientation is lost we plot in Fig. 21, panels A and B, the orientation correlation function  $K(\mathbf{r}_1 - \mathbf{r}_2)$ , defined by Eq. (9).

A crucial observation is that the correlation falls off very fast being almost zero at the intervortex distance. This result supports Nemorivskii's Gaussian model of  $^4\text{He}$ -vortex tangle [58], in which correlation of the orientations disappears at inter-vortex distance  $\ell$  and the mean loop length  $\bar{L} \gg \ell$ .

Interestingly, for weak counterflow velocities  $V_{\text{ns}} = 0.5$  cm/s there is a distinct negative correlation (the segments are anti-parallel) at distances just beyond  $\ell$ . This can be related with the tendency of close vortex lines to become antiparallel on the way to reconnection. For stronger  $V_{\text{ns}} = 1$  cm/s, i.e. in more dense tangles, this tendency is masked by the influence of other neighboring vortex lines. Therefore such an anti-parallel orientation is not observed.

Averaging these correlation functions over all distances we find that on average the tangle is slightly polarized and this polarization  $K$  depends on the intervortex distance  $\ell$ , but not on the temperature: see Fig. 21C where we plot  $K$  as a function of  $\ell$  for three temperatures. The value of  $\ell$  at given  $T$  was varied by the counterflow velocity. Here again there is no noticeable difference in the values and dependencies of  $K(\mathbf{r}_1 - \mathbf{r}_2)$  and  $K$  for different reconnection criteria, therefore only GEC case is displayed.

The most important observation in Fig. 21C is that  $\bar{K} \sim 10^{-3}$  i.e. is vanishingly small with respect to unity. This means that there is no coherent contribution (of many vortex lines) to the velocity field at large scales (much above  $\ell$ ). Therefore the energy spectrum of the turbulent vortex tangle,  $E(k)$ , has to be determined by contributions of individual vortex lines even for  $k\ell \ll 1$ , up to the box size.

## VI. ON THE PHYSICS OF $^4\text{HE}$ COUNTERFLOW TURBULENCE

In this section we present a summary of the result obtained here and in other studies of counterflow turbulence.

### A. Idealizations and relevant parameters

#### 1. Spatial homogeneity

In analogy to classical hydrodynamic turbulence, the basic models of counterflow turbulence are based on the assumption of spatial homogeneity of the problem. In laboratory experiments on counterflow in  $^4\text{He}$  this can be realized to some extent in a wide channel or a pipe of transverse size  $H$  that significantly exceeds the intervortex distance  $\ell$ . For example, in the super flow experiments of Ref. [17] the largest  $H = 1$  cm, while

$\ell$  varies (approximately) from 0.1 to  $4 \cdot 10^{-4}$  cm (for  $V_{\text{ns}} \simeq 20$  cm/s).

In numerical simulations (like ours) the homogeneity can be simply reached with periodic boundary conditions. Again the size of the box  $H$  (cube in our case) should be larger than  $\ell$ . In our simulations  $H = 0.1$  cm, while  $\ell$  varies from 0.005 cm to 0.04, as seen in Fig. 5.

One additional simplifying assumption made in our study (and many others) is that the flow of the normal component is laminar. In numerical simulations (including ours) this simply requires  $V_{\text{n}} = \text{const}$ . In experiments this is achieved to some extent in a core of a wide-channel counterflow, when  $V_{\text{ns}}$  is below some critical value  $V_{\text{cr}}$ , above which the normal fluid flow is expected to become turbulent. Probably a better realization of the laminarity assumption in laboratory experiments is achieved in the "pure" super flow, where normal fluid flow is prevented by super leaks, a kind of (e.g. silver) porous medium with sub-micron size pores to prevent a net flow of the viscous normal component through the channel on any experimentally relevant flow time scale, see e.g. Ref. [17]. Now, if one neglect the  $V_{\text{n}}$  dependence on the (transverse) distance to the wall, the entire problem can be approximated as spatially homogeneous.

In order to relax the assumption of space homogeneity one has to develop a theory (or a model) of superfluid wall-bounded flow which will find and account for an actual laminar super- and normal-fluid velocity profiles across a channel. This is still an open problem. Even more sophisticated and challenging open problem is a superfluid wall-bounded turbulence at large counterflow velocities, when both the normal and the superfluid components are turbulent and their mean-velocity and turbulent-energy profiles have to be found self-consistently, accounting for the mutual friction between the components. Detailed information about the vortex tangle structure, found and analyzed in this paper, is required to successfully approach this problem. This was one of the important motivations for the present study.

#### 2. No isotropy, just axial symmetry

It is generally accepted that the classical hydrodynamic turbulence is almost isotropic at small scales  $l \ll H$  due to the isotropization effect that is observed going from the outer scale  $H$  toward the small scales  $l$ . The theory of small scale turbulence then simplifies. In the counterflow case there is no energy cascade and the superfluid counterflow turbulence is inherently anisotropic due to the built-in direction of the counterflow velocity  $\mathbf{V}_{\text{ns}}$ . This anisotropy is of principal importance and cannot be ignored at all. Indeed, in the isotropic case there is no friction force between the normal- and superfluid components and the counterflow does not create a vortex tangle. One can formally see this from the following argument: consider the parameter  $C_f$  that quantifies the

mutual friction and  $\gamma$  that determines the vortex tangle density (Sects. IV A 4 and IV E). Both are proportional to the anisotropy parameter  $I_\ell$ , which is equal to zero in the isotropic tangle.

Nevertheless, in a spatially homogeneous case with the only relevant direction  $\mathbf{V}_{\text{ns}}$  one expects to see axial symmetry around  $\mathbf{V}_{\text{ns}}$ . Indeed, in our simulations the coefficient  $I_{\ell\perp}$  [defined by Eq. (4d)], which is responsible for the axial asymmetry, is close to zero.

### 3. The physical parameters of the problem

The main parameter in the problem of quantum turbulence is the circulation quantum  $\kappa \approx 10^{-3} \text{ cm/s}^{-2}$ .

The second parameter is the vortex core radius  $a_0$ . In  $^4\text{He}$   $a_0 \simeq 10^{-8} \text{ cm}$ . In the theory of counterflow turbulence  $a_0$  appears in the combination with the intervortex distance  $\ell$  as a dimensionless parameter  $\Lambda \simeq \ln(\ell/a_0)$ . More accurate definition of  $\Lambda$  is given by Eq. (11), where we also introduced  $\tilde{\Lambda} = \Lambda/(4\pi)$ . The parameter  $\tilde{\Lambda}$  naturally appears in the equations of motion for the vortex line in the local induction approximation. Table I shows that in actual experimental situations  $\tilde{\Lambda}$  is very close to unity.

Additional dimensionless parameters are  $\alpha$  and  $\alpha'$  which determine the mutual friction force [according to Eq. (10b)]. Of the two  $\alpha$  is more important, being responsible for the dissipative part. As one sees in Tab. I,  $\alpha$  varies in the relevant temperature range by a factor of 8, being much smaller than unity ( $\alpha = 0.036$ ) at  $T = 1.3$  and approaching unity, when  $T$  is close to  $T_\lambda$ , see Tab. I.

We have also to mention the ratio of normal and superfluid densities  $\rho_s/\rho_n$ . Having in mind that the total  $^4\text{He}$  density  $\rho \equiv \rho_s + \rho_n$  in the problem at hands can be considered as temperature independent we can use the ratio  $\rho_n/\rho$  instead of  $\rho_s/\rho_n$ . It varies about ten times (from 0.045 to 0.42, see Tab. I) in the studied temperature range.

Having so many dimensionless parameters that essentially deviate from unity and vary significantly with temperature, one may think that dimensional reasonings are useless in our problem. However, as we have shown in the paper, they are still useful. Being supplemented with simple physical arguments they give quite reasonable results, for example to determine the  $V_{\text{ns}}$  dependence of the basic tangle characteristics, see below.

### B. $V_{\text{ns}}$ -dependence of the vortex-tangle characteristics

Using dimensional reasoning with the only parameter  $\kappa$  we reproduced a set of relationships that determined

the  $V_{\text{ns}}$ -dependence of the main characteristics of the vortex tangle. For concreteness, we list them in the order of increasing powers of  $V_{\text{ns}}$  and remind the values of corresponding dimensionless parameters:

The mean and RMS vortex line curvature,  $\bar{S} = c_1/\ell \propto V_{\text{ns}}^{-1}$ ,  $\tilde{S} = c_2/\ell \propto V_{\text{ns}}^{-1}$ , see Eqs. (5), Fig. 12 and Tab. IV;  $c_2 \approx \sqrt{3/2} c_1 \simeq 2 \div 3$ .

The anisotropy indices  $I_{\parallel}$ ,  $I_{\perp}$ ,  $I_\ell$  and  $I_{\ell\perp}$  are practically independent of  $V_{\text{ns}}$ , i.e.  $\propto V_{\text{ns}}^0$ , see Eqs. (4), Fig. 11 and Tab. IV;  $I_{\parallel}$ ,  $I_{\perp} \simeq 0.7 \div 0.9$ ,  $I_\ell \simeq 0.5$ ,  $I_{\ell\perp} \approx 0$  (because of the axial symmetry).

The drift velocity  $V_{\text{vt}} = C_{\text{vt}} V_{\text{ns}}$ , see Eq. (7b), Fig. 13;  $C_{\text{vt}} \simeq 0.05 \div 0.08$ .

Vortex line density  $\mathcal{L} = \kappa^2 (\Gamma V_{\text{ns}})^2$ , see Eq. (2a), Fig. 8 and Tab. III;  $\Gamma \simeq 0.07 \div 0.16$ .

The mutual friction force density,  $F_{\text{ns}} = \alpha \rho_s \kappa^{-1} (C_f V_{\text{ns}})^3$ , see Eq. (8b), Fig. 14; The derivation of Eq. (8b) was based not only on dimensions of  $F_{\text{ns}}$  but also on its explicit expression (8a) via configuration of the vortex tangle;  $C_f \simeq 0.15 \div 0.25$ .

The reconnection rate  $dN_r/dt = c_r \kappa \mathcal{L}^{5/2} \propto V_{\text{ns}}^5$ , see Eqs. (3) and (2a), Fig. 7 and Tab. II;  $c_r \simeq 0.4 \div 0.6$ .

As one sees in the figures mentioned above, the results of our numerical simulations agree well with all these expected  $V_{\text{ns}}$  dependencies. Notice that the numerical values of the corresponding dimensionless parameters (presented above) are not always of the order of unity but often smaller by an order of magnitude. Some understanding of the reason for that can be obtained with the explicit form of the bridge relations of Schwartz's obtained using the local interaction approximation as discussed next.

### C. Schwartz's bridge relations

Using the equation of motion (11) in the local interaction approximation Schwartz [19] analytically derived the bridge relations that connect some of the parameters mentioned above. In our dimensionless notations these are:

$$\Gamma_s \equiv \kappa \gamma_s \approx \frac{I_\ell}{\Lambda c_2^2} \quad [\text{by comparing Eqs. (2a) and (19)}].$$

Equation (20) for  $C_{\text{vt}}^{\text{LIA}}$  that quantifies the tangle drift velocity  $V_{\text{vt}}$  [see Eq. (7b)].

Equation (21) for  $C_f^{\text{LIA}}$  that quantifies the mutual friction force density  $F_{\text{ns}}$  [see Eq. (8b)].



These equations bridge  $\Gamma_s$ ,  $C_{vt}^{LIA}$  and  $C_f^{LIA}$  with the tangle anisotropy parameters  $I_{||}$ ,  $I_\ell$ , defined by Eqs. (4) and tangle RMS curvature parameter  $c_2$ , defined by Eqs. (5).

These bridge relations are fulfilled with reasonable accuracy in our simulations (with the full Biot-Savart equation), especially for low temperatures. For higher temperatures the discrepancy increases, but overall the order of magnitude of these coefficients is close to those calculated by Schwarz (with  $I_{||}$ ,  $I_\ell$  and  $c_2$  obtained by LIA simulations) and agree with available experimental data. This allows us to believe that the Local-Induction Approximation may be successfully used in analytical studies of counterflow turbulence in spite of the fact that it fails in numerical simulations.

#### D. Probability distribution and correlation functions in the vortex tangle

Many of the mean parameters discussed above can be measured experimentally, at least in principle. However detailed statistical information of the random vortex tangle statistics is hardly expected in foreseeable experiments. Because of their importance for better understanding the basic physics of counterflow turbulence we put some efforts to clarify it numerically. In particular, we studied:

The PDF of the vortex-loop length  $\mathcal{P}(l)$  and showed that its core (that contains about 20 ÷ 30% of the total loops) can be described by a simple exponential form (22) as seen in Fig. 17A. It has a peak at some  $L_* \sim 0.01 \div 0.02$  cm, which is much smaller than the mean loop length  $\bar{L} \sim 0.3 \div 0.5$  cm, defined by the tail of the PDF, see Fig. 16.

The correlation between the length  $l_j$  and the RMS curvature  $\tilde{s}''_j$  of loops with a given  $l_j$  is demonstrated in Fig. 19. We show that for long loops  $\tilde{s}''_j$  is practically independent of their length and close to the overall RMS curvature  $\tilde{S}$ , while for short loops its bounded from below by (and concentrated close to) the curvature of a circle with a given length.

The PDF of the line curvature  $\mathcal{P}(|s''|)$ . We show that  $\mathcal{P}(|s''|)$  may be well described by an exponential form (23) without fitting parameters, just involving the RMS curvature  $\tilde{S}$ . This allowed us to find the ratio between the structural parameters  $c_1/c_2 \approx \sqrt{2/3}$ .

The PDFs of the mean and the RMS loop curvature. We show that more than 90% of the PDF are close to a Gaussian form (25) and studied in Sec. VD the temperature dependence of their maxima and widths.

Last but not least: the characteristics of the vortex tangle in the form of the autocorrelation function of

the vortex orientation  $K(\mathbf{r})$ , defined by Eq. (9). Figures 21 shows that  $K(\mathbf{r})$  practically vanishes at distances about  $\ell$ . This means that vortex lines is reminiscent of a random walk with a correlation length of the order of the intervortex distance. This fact has many important consequences, e.g. for the energy spectra in counterflow turbulence.

#### E. Dynamical and statistical characteristics vs. reconnection criteria

We carried out full Biot-Savart simulations of the evolution of the vortex tangle within the vortex filament method in a wide range of parameters. We compared the statistical and geometrical properties of the dense tangles using three different reconnection criteria (geometrical G, geometrical-energetic GE and dynamical D) and identified which properties are robust and which are sensitive to the choice of the criterion. We found the following:

The reconnection rate is a property directly related to the choice of the criterion. We concluded that the reconnection rate is similar for **GE** and **D** criteria albeit their different physical interpretations. On the other hand, in simulations with **GC** the reconnection rate is significantly higher. The detailed analysis shows that most of the reconnections according to **GC** lead to an increase of the total length and to the creation of a very large number of small loops and loop fragments. The small loops removal procedure is therefore an essential part of the algorithm for this criterion.

One of the main parameters,  $\mathcal{L}$ , depends on the choice of the reconnection criterion for high temperature and strong counterflow velocities, when the tangle become dense. **GC** lead to sparser tangle, while **DC** gives the most dense tangle for the same  $T$  and  $V_{ns}$ . As a consequence, the coefficient  $\gamma$  differs beyond measurement errors. Our results for  $\gamma$  agree well with available data. Thus the sensitivity of  $\mathcal{L}$  to the choice of the reconnection criterion may explain the spread of the results for  $\gamma$  as found in literature.

In agreement with previous studies we found that the vortex tangle is oblate and isotropic in the direction perpendicular to the counterflow. We observed a slight  $V_{ns}$  dependence of  $I_{||}$  for  $T = 1.6$  and  $1.9$  K for **G** and **GE** criteria. For all temperatures the tangle was most oblate for **GC** and least oblate for **DC**.

The tangle drift velocity and the mutual friction force density depend on the choice of the reconnection criterion at moderate and high temperatures, with the corresponding coefficients being largest for **DC** and smallest for **GC**. This is similar to the behavior of the vortex line density.

The local tangle structure – the mean and RMS curvature of the tangle as well as PDFs of the loops length and curvatures – are only slightly dependent on the reconnection criterion.

The autocorrelation of the vortex orientation is practically independent of the choice of the reconnection criterion.

Despite some clear differences in some results obtained with different reconnection criteria, vortex filament methods may be considered robust and well suited for the description of the steady state vortex tangle in the counterflow provided the results are interpreted having in mind the found values of the spread due to particular details of implementation.

\*\*\*

We believe that the numerical results obtained in this paper and their analysis will help in further studies of counterflow turbulence.

### Acknowledgments

This paper had been supported in part by the Minerva Foundation, Munich, Germany and by the grant 13-08-00673 from RFBR (Russian Foundation of Fundamental Research). LK acknowledges the kind hospitality at the Weizmann Institute of Science during the main part of the project. We are grateful to W.F. Vinen and L. Skrbek for their important comments, criticism and suggestions. We also thank S. K. Nemirovskii, N. J. Zabusky and P. Mishra for their comments on the manuscript.

- 
- [1] Blazkova M., Schmoranzler D. and Skrbek L., *Phys.Rev. E*, **75**, (2007) 025302.
- [2] Charambolous D., Skrbek L., Hendry P. C., McClintock P. V. E. and Vinen W. F., *Phys. Rev.E*, **74** (2006) 036307.
- [3] Jager J., Schuderer B. and Schoepe W., *Phys. Rev.Lett.*, **74**, (1995) 566.
- [4] Stalp S. R., Skrbek L. and Donnelly R. J., *Phys.Rev. Lett.*, **82** (1999) 4831.
- [5] Fuzier S., Baudouy B. and Van Sciver S. W., *Cryogenics*, **41** (2001) 453.
- [6] Y. Nago, T. Ogawa, A. Mori, Y. Miura, K. Obara, H. Yano, O. Ishikawa, T. Hata, Observation of Remanent Vortices Attached to Rough Boundaries in Superuid 4He, *J. Low. Temp. Phys.*, 158, 443 (2010).
- [7] Maurer J. and Tabeling P., *Europhys. Lett.*, **43** (1998) 29.
- [8] Roche P.-E., Diribarne P., Didelot T., Français O., Rousseau L. and Willaime H., *EPL*, **77** (2007) 66002.
- [9] W. F. Vinen, Mutual Friction in a Heat Current in Liquid Helium II. I. Experiments on Steady heat Current, *Proc. R.Soc. Lond. A* **240**, 114 (1957); II. Experiments on Transient Effects, *Proc. R.Soc. Lond. A* **240**, 128 (1957); III. Theory of the Mutual Friction, *Proc. R.Soc. Lond. A* **243**, 400 (1957).
- [10] F. Vinen, Mutual Friction in a Heat Current in Liquid Helium II. IV. Critical Heat Currents in Wide Channels, *Proc. R. Soc. Lond. A* 1958 **243**, 400 (1958).
- [11] R.T. Wang, C.E.Swanson, and R.J. Donnelly, *Phys.Rev.B*, 36, 5240 (1987).
- [12] R. K. Childers and J. T. Tough, Helium II thermal counterflow: Temperature- and pressure-difference data and analysis in terms of the Vinen theory, *Phys.Rev.B.*, **13**, 1040 (1976).
- [13] J.T. Tough, Superfluid turbulence, *Progress in low temperature physics*, **VIII**, 133 (1982)
- [14] Zhang T. and Van Sciver S., *Nat. Phys.*, 1 (2005) 36.
- [15] Zhang T. and Van Sciver S., *J. Low Temp. Phys.*, **138**(2005) 865.
- [16] Barenghi C. F., Gordeev A. V. and Skrbek L., *Phys. Rev. E*, **74** (2006) 026309.
- [17] S. Babuin, M. Stammeier, E. Varga, M. Rotter, and L. Skrbek, Quantum turbulence of bellows-driven 4He superflow: Steady state, *Phys. Rev. B* **86**, 134515 (2012).
- [18] K. W. Schwarz, Three-dimensional vortex dynamics in superfluid  $^4\text{He}$ : Line-line and line-boundary interactions. *Phys. Rev.B*, **31**, 5782 (1985).
- [19] K. W. Schwarz, Three-dimensional vortex dynamics in superfluid  $^4\text{He}$ : Homogeneous superfluid turbulence, *Phys. Rev.B*, **38**, 2398 (1988).
- [20] A.T.M. de Waele and R.G.K.M Aarts, Route to vortex reconnection, *Phys. Rev. Lett.*, **72**, 482 (1994)
- [21] R.G.K.M Aarts and A.T.M. de Waele, Numerical Investigation of the flow properties of He II. *Phys. Rev. B*, **50**, 10069 (1994).
- [22] Hiroyuki Adachi, Shoji Fujiyama, and Makoto Tsubota, Steady-state counterflow quantum turbulence: Simulation of vortex filaments using the full Biot-Savart law, *Phys. Rev. B* **81**, 104511 (2010)
- [23] R. A. Ashton, L. B. Opatowsky, and J. T. Tough, *Phys. Rev. Lett.* 46, 658 (1981)
- [24] C.F. Gorter and J. H. Mellink, *Physica* **27**, 924 (1041)
- [25] L. Skrbek and K. R. Sreenivasan, Developed quantum turbulence and its decay, *Physics of Fluids* **24**, 011301 (2012).
- [26] Makoto Tsubota, Michikazu Kobayashi, Hiromitsu Takeuchi, *Physics Reports*, **522**, 191 (2013)
- [27] Sergey K. Nemirovskii, *Physics Reports*, **524**, 85 (2013)
- [28] David C. Samuels, *Phys. Rev B* **46** 11714 (1992)
- [29] J. Koplik and H. Levine, *Phys. Rev. Lett.* **71**, 1375 (1993);
- [30] R. Tebbs, A. J. Youd, and C. F. Barenghi, *J. LowTemp. Phys.* **162**, 314 (2010);
- [31] M. Leadbeater, T. Winiecki, D. C. Samuels, C. F. Barenghi, and C. S. Adams, *Phys. Rev. Lett.* **86**, 1410 (2001).
- [32] S. Nazarenko, R. West, Rapid Communication, Analytical solution for nonlinear Schroedinger Vortex reconnection, *J. Low Temp. Phys.* 132,1 (2003).
- [33] S. Ogawa, M. Tsubota, and Y. Hattori, Study of reconnection and acoustic emission of quantized vortices in su-

- perfluid by the numerical analysis of the Gross-Pitaevskii equation, *J. Phys. Soc. Jpn.*, **71**, 813 (2002).
- [34] MS Paoletti, ME Fisher, DP Lathrop, Reconnection dynamics for quantized vortices, *Physica D: Nonlinear Phenomena* **239**, 1367-1377 (2010)
- [35] D. Kivotides, Spreading of superfluid vorticity clouds in normal-fluid turbulence, *J. Fluid Mech.*, **668**, 58 (2011)
- [36] D.C. Samulels and D. Kivotides, A Damping Length Scale for Superfluid Turbulence, *Phys. Rev. Lett.*, **83**, 5306 (1999).
- [37] Makoto Tsubota, Tsunehiko Araki, and Sergey K. Nemirovskii, Dynamics of vortex tangle without mutual friction in superfluid  $^4\text{He}$ , *Phys. Rev. B*, **62**, 11 751(2000).
- [38] Luiza P. Kondaurova, Sergey K. Nemirovskii, *J. Low temp. Phys.*, **138**, 555 (2005)
- [39] Luiza P. Kondaurova, Vladimir A. Andryuschenko, Sergey K. Nemirovskii, Numerical Simulations of Superfluid Turbulence under Periodic Conditions, *J Low Temp Phys* **150**, 415 (2008).
- [40] Luiza P. Kondaurova, Vladimir A. Andryuschenko, Sergey K. Nemirovskii, Numerical simulations of the dynamics of vortex tangle in superfluid helium (in Russian), *Vychislitel'nye tehnologii*, **15**, 45 (2010).
- [41] A. Baggaley, The Sensitivity of the Vortex Filament Method to Different Reconnection Models, *J. Low Temp. Phys.* **168**, pp. 18-30 (2012)
- [42] C.F. Barenghi, D.C. Samuels, Scaling laws of vortex reconnection, *JLTP*, **156**, 281 (2004)
- [43] Sergey K. Nemirovskii, Evolution of a Network of Vortex Loops in He-II: Exact Solution of the Rate Equation PRL, **96**, 015301 (2006).
- [44] D.R. Poole, H. Scofield, C.F. Barenghi, D.C. Samuels, Geometry and Topology of Superfluid
- [45] Ronald Aarts, Ph.D Thesis, A numerical study of quantized vortices in HeII, Technische Universiteit Eindhoven, 1994. *Turbulence, J. Low Temp. Phys.*, **132**, 97 (2003).
- [46] F. R. Hama, *Phys. Fluids* **6**, 526 (1963); R. J. Arms and F. B. Hama, *Phys. Fluids* **8**, 553 (1965).
- [47] K. W. Schwarz, *Phys. Rev. Lett.* **49**, 283 (1982)
- [48] G.W. Rayfield and F. Reif, *Phys. Rev.* **136**, A1194 (1964)
- [49] R. J. Donnelly and C. F. Barenghi, *J. Phys. Chem. Ref. Data*, **27**, No. 6, (1998)
- [50] W.H. Press, B.P. Flannery, S.A. Teukolsky, W.T. Vetterling, *Numerical Recipes, The Art of Scientific Computing*, Cambridge University Press, New York, USA, 1986
- [51] K. P. Martin and J. T. Tough, *Phys. Rev. B* **27**, 2788 (1983)
- [52] Y. Minoda, M. Tsubota and W.F. Vinen, *J. Low Temp. Phys.*, **171**, 511 (2013).
- [53] Bauerle et al., *Nature* **382**, 332 (1996), C. Winkleman PhD Thesis, J. Elbs, PhD Thesis (2007).
- [54] D.D. Awschalom, F.P. Miliken, and K.W. Schwarz, *Phys. Rev. Lett.* **53**, 1372 (1984)
- [55] V. Arp, *Cryogenics*, **10**, 96 (1970)
- [56] H.C. Kramers, T. M. Wiarda, and A. Broese van Groenou, *Proc. LT7*, p. 562. (University of Toronto Press, 1961); H.C. Kramers, in *Superfluid Helium*, p. 199, ed. J. F. Allen (Academic, London, 1965)
- [57] C. E. Swanson and R. J. Donnelly, *J. Low Temp. Phys.* **61**, 363 (1980).
- [58] S.K. Nemirovskii, *Phys. Rev. B*, **57**, 5972 (1998).